Paper Ref: acp-2020-456

Title: " Determination of the absorption cross-sections of higher order iodine oxides at 355 nm and 532 nm"

RESPONSE TO THE REPORT OF REVIEWER #1

We are grateful to the reviewer for helpful and constructive comments and suggestions. We address them point by point below. The Reviewer's comments are shown in bold typescript, our response in normal typescript. Changes to the manuscript are highlighted in red. Page numbers refer to the revised manuscript.

Lewis et al combine experimental and theoretical work examining the absorption cross-sections of higher iodine oxides (IxOy). The results indicate that most oxides are rapidly removed by photolysis, which has repercussions for formation of iodine containing particle. The experiments are complex as IxOy have to be generated in-situ, the data appears to be of reasonable quality. This review does not address the accuracy of the theoretical work. The manuscript is well written; the authors may consider the following suggestions for improvement.

Main comment: Actinometry at 355 nm is using NO2 whereas OIO is used at 532 nm. The absorption cross-section of OIO at 532 nm is quoted as being "relatively well known" (L174). The cross-sections of I2 are well known as are those of NO2. It is questionable whether an unstable trace-gas, the spectrum of which has only been measured following its transient formation as the product of the IO-self reaction can be termed "well known". The authors must be more quantitative here. They should properly review (and cite) the limited literature on the OIO cross-section at this wavelength. The same applies to the unity quantum yield of photolysis of OIO. Do all the literature studies agree on this value? Again, the authors need to review (and cite) the literature and state why they believe the quantum yield is one, rather than simply citing one article in which one of the present authors also contributed.

A problem with using I_2 as an actinometer is that its spectrum has many rovibrational lines around 532 nm, and therefore the cross sections determined at this wavelength are very resolution-dependent. Thus, we would have had to determine the absorption cross section of I_2 for our specific laser line width (1 cm^{-1} or 0.03 nm). A second problem specific to our PI-ToF-MS detection system is that I_2 photoionizes very efficiently at 118 nm (see section 2.1), which causes an overload in the detector from the I_2 peak signal towards longer flight times (i.e. higher masses) and requires gating the peak. We have nevertheless carried out a test with partial gating of the I_2 peak. In this test, I_2 depletion was (17 ± 5)% and OIO depletion was (54 ± 4)%. Using the I_2 cross section at 532 nm determined by Tucceri et al. (2006) at 1.4 cm^{-1} resolution (0.04 nm), we obtain $\sigma_{OIO} = (8 \pm 3) \times 10^{-18}$ cm^2 $molecule^{-1}$, which is fully consistent with the literature values of the absolute absorption cross sections of OIO listed in the table below, lending confidence to the method. The main source of uncertainty in this determination is the noise in the semi-gated I_2 trace.

Reference	**Resolution /nm**	**σ_{OIO} /cm^2 $molecule^{-1}$**
Joseph et al. (2005)	0.006	567.93 nm: $(1.51 \pm 0.18) \times 10^{-17}$ 532 nm*: 1.25×10^{-17}
Gomez Martin et al. (2005) Spietz et al. (2005)	0.35 1.3	549.2 nm: $(1.3 \pm 0.3) \times 10^{-17}$ 549.2 nm: $(1.1 \pm 0.3) \times 10^{-17}$ 532 nm: 8.9×10^{-18}
Tucceri et al. (2006)	0.04	610 nm: $(6 \pm 2) \times 10^{-18}$ 532 nm*: 8.2×10^{-18}
Bloss et al. (2001)	1.13	549.2 nm: $(1.1 \pm 0.2) \times 10^{-17}$ 532 nm: 9.9×10^{-18}

The cross sections at 532 nm with an asterisk have been obtained by scaling the relative spectrum measured by Spietz et al. to the cross section of that study at the corresponding wavelength. The relative cross sections measured by Spietz et al. and Bloss et al. are in good agreement, as shown by the selected peak-to-valley ratios listed in the following table:

Reference	**σ_{OIO}(532.0 nm)/σ_{OIO}(541.2 nm)**	**σ_{OIO}(549.2 nm)/σ_{OIO}(560.3 nm)**
Spietz et al. (2005)	2.7 ± 0.2	3.2 ± 0.2
Bloss et al. (2001)	2.2 ± 0.2	3.0 ± 0.2

Considering the differences in methods, resolution and wavelength of the different determinations of the OIO cross sections listed above and the reported uncertainties, the agreement can be considered as reasonable and the cross section at 532 nm can be considered as well stablished, at least within 25%.

There are essentially two independent experimental determinations of the OIO photolysis quantum yield above 500 nm (Tucceri et al. 2006 and Gomez Martin et al. 2009). The studies by Tucceri et al. 2006 and Gomez Martin et al. 2009 employed similar methods and performed similar tests. The main problem of the reaction scheme used by Tucceri et al. in the detection of I atoms was the presence of high ozone concentrations ($\geq 10^{16}$ molecule cm^{-3}), which most likely reduced the lifetime of the I atom photofragment to tens of microseconds, besides other experimental complications such as formation of I_2 and aerosol. In the absence of O_3, Gomez Martin et al. observed a long-lived I photofragment and no reformation of OIO (on a time scale of several ms), strongly suggesting that OIO does indeed photolyze to I + O_2. Further evidence supporting a unit photolysis quantum yield comes from the short lifetime (200 fs) of the C^2A_2 excited state, determined by Ashworth et al. (2002) through simulations of the rotational envelopes of the observed absorption bands. A high-level MRCI theoretical study of the OIO excited states by Kirk Peterson (2010) found a low barrier for dissociation to I + O_2 for the A^2B_2 state, which should lead to efficient I atom production via an initial spin–orbit interaction between the C^2A_2 state and the nearby B^2A_1, followed by a strong vibronic interaction with the A^2B_2 state via an avoided crossing.

Insertion in Page 9, Line 225: The use of I_2 as actinometer is also precluded by the overload issue mentioned above. The OIO absorption cross section at 532 nm is relatively well known, within 25% of the average value of the four independent determinations reported in the literature (Bloss et al., 2001; Joseph et al., 2005; Spietz et al., 2005; Tucceri et al., 2006). On the other hand, conflicting results have been reported for the OIO photolysis quantum yield (Tucceri et al., 2006; Gomez Martin et al., 2009). Here we use the unit quantum yield reported by Gomez Martin et al. (2009), which was determined in a system free of interferences from ozone where a long-lived I atom photofragment and no reformation of OIO was observed over a time scale of several milliseconds. This result is also supported by the short lifetime (200 fs) of the excited state responsible for the observed absorption bands (Ashworth et al., 2002) and the existence of a feasible photolysis path revealed by high level ab initio calculations (Peterson, 2010).

L31 Presumably the 9-16% ozone depletion from iodine chemistry refers to the marine boundary layer. This should be made clear.

This % is indeed over the integrated tropical troposphere as indicated in the cited reference and a new reference added: https://www.atmos-chem-phys.net/16/1161/2016/

L77 “This is currently an important uncertainty. . .” What does “this” refer to? Perhaps “an important source of uncertainty” is better?

Amended in text

L114 Signal-to-noise ratio ~ 400. S/N measured over what period of time? Is drift in laser intensity not more important than S/N for an absorption cell that has no reference photo-diodes. Limit of detection in OD units would be more useful.

The signal from the photodiode was accumulated over ~15 seconds. It is true that the laser intensity drifts, however the drift was not significant over this time period. The S/N increases quickly over ~15 s, before plateauing, and eventually decreasing due to the drift in intensity. Signals were measured back-to-back, so as to negate intensity drift as much as possible. The back-to-back measurements were carried out until 3 concordant results (OD variation <10%) were obtained, which is typically the first 3 results.

Insertion in Page 5, Line 121: […] which corresponds to a minimum detectable OD of 2.5E-3. As there is no reference photodiode in this setup, drift in laser intensity must be accounted for. To negate the effect of laser drift as much as possible, the probe intensity is measured over a period of 15 seconds for both I and I_0, with ~10s between the measurements. To ensure that laser drift does not significantly affect the measured concentrations, measurements are taken until 3 concordant results are obtained (typically the first three results).

Figure 4. What is the pulse-width of the excitation laser ? Please explain why the depletion of NO2 (presumably in ~10 ns) takes 150 ms until the new plateau is reached. To which expression was the red curve fitted and why was it chosen?

The specified pulse width of the Continuum Surelite 10-ii is 3-5 ns. The depletion time of 150 **microseconds** is a sampling time and results from transport of molecules between the region where they are photolyzed to the region where they are photoionized. The sampling in this system can be described in the following steps:

i) Transport of molecules from the reactor toward the sampling orifice.
ii) Transport of the molecules through the sampling orifice.
iii) Transport of the molecules from the exit of the sampling orifice to the ionization region.

The sampling time depends on the alignment of the lasers and on the molecular masses of the bath gas and sample species (Baeza-Romero et al., 2011, DOI: 10.1002/kin.20620).

The curve chosen is a sigmoidal curve with variable Hill slope given by parameter 'p'.

$$y = S_0 + \frac{S_1 - S_0}{1 + 10^{(\log x_0 - x)p}}$$

This fitting function is chosen to fit empirically the observed depletion curves. The only parameters relevant to this study are the top and bottom asymptotes.

Insertion in Page 8, Line 169: The trace shown in Figure 4, which is similar to all the traces obtained in this experiment, exhibits a delay between the pre- and post-photodepleted signal. This delay corresponds to an instrumental sampling time depending on the alignment of the lasers and the molecular masses of the bath gas and the sample species (Baeza-Romero et al., 2012). In the present experiments, it was necessary to leave a small gap (~2 mm) between the photolysis volume and the sampling pinhole, so as to avoid hitting the skimmer cone with the laser. The diffusional exchange of molecules between the photodepleted volume, and the un-photodepleted volume immediately before the pinhole blurs the onset of the photodepletion as it is measured by the TOF-MS. The values of S_0 and S_1 were obtaining by empirically fitting the photodepletion trace to a sigmoidal function:

$$y = S_0 + \frac{S_1 - S_0}{1 + 10^{(\log x_0 - x)p}} \qquad (2)$$

Fitting to this function ensures that the flat sections corresponding to the pre- and post-photodepletion concentrations (S_0 and S_1 respectively) are characterized in the precise regions outside of the aforementioned "blurred" zone. The parameters x and p are not of scientific importance for this study and are simply instrumental factors.

L146 and L147 Laser "shot", excimer "flash". Perhaps use the term "pulse" ?

Agreed that pulse is better, changed in the text

Figure 6 What causes the increase in the IO signal after 1.85 ms.

Photolysis of IO at 355 nm results in O and I atoms, which will react respectively with I_2 and O_3 in the reaction mixture rapidly, reforming some of the IO lost to photodepletion. In addition, some O_3 may also photolyze at 355 nm producing O atoms.

L259 Please show the trace obtained using the actinometer (OIO). This could potentially go into supplementary information along with the raw data (lack of signal change) for the higher oxides and would give the reader an idea of the data-quality.

Added as new Figure 8.

Figure 7 Indicate when the laser was triggered in the I2O3 experiment. Are the red curves the same function as used in Figure 4 ?

Now indicated in the figure caption.

Yes, all traces are analysed by performing the same empirical fit. This is now stated in page 8.

L370 please provide references to the tropical UTLS being a "hotspot" of iodine chemistry. Have there been measurements of IO or higher iodine oxides in this part of the atmosphere?

Yes, the reference was already there a few sentences later. We have inserted the reference (Koenig et al., PNAS 2020) at the beginning of the paragraph. However, calling the UTLS a 'hotspot' may lead to think of places like Mace Head, Antarctica, etc. Therefore, we refer now to the UTLS as an 'active iodine chemistry region' instead.

Paper Ref: acp-2020-456

Title: " Determination of the absorption cross-sections of higher order iodine oxides at 355 nm and 532 nm”

RESPONSE TO THE REPORT OF REVIEWER #2

We are grateful to the reviewer for helpful and constructive comments and suggestions. We address them point by point below. The Reviewer’s comments are shown in bold typescript, our response in normal typescript. Changes to the manuscript are highlighted in red. Page numbers refer to the revised manuscript.

Review of “Determination of the absorption cross-sections of higher order iodine oxides at 355 nm and 532 nm” by Lewis et al. This paper presents photochemical data for iodine oxides (IxOy), a hitherto elusive family of atmospheric transients thought to play an important role in the coastal marine boundary layer. Results were determined via laser photolysis / photodepletion experiments using mass-spectrometry detection of IxOy, supplemented by ab-initio calculations. This first extensive dataset can provide valuable information needed to construct models of atmospheric chemistry. However, there were a few points that require further clarification and discussion within the manuscript prior to publication in ACP.

Firstly, experiments appear to have been conducted under very different conditions of gas pressure and identity to those found in the boundary layer. At the top of page 6 it was stated that experimental pressures of 4 to 7 Torr were used (though whether of He or N2 was not clear). This is clearly a very different matrix of gases to 760 Torr of N2, O2 and H2O found in coastal boundary layer air. There is surely some doubt therefore, whether some qualitative observations from this work are valid for atmospheric models. The chemical mechanisms for IxOy formation will surely differ to some extent due to changes in stabilization rates for association products at the different gas-pressure, or perhaps reactions of transients with O2 (or even H2O) that would proceed faster in the boundary layer. Specifically, much is made of the absence of I4Oy species, but we simply do not know if these compounds would be formed in realistic atmospheric conditions. If there is clear evidence for why such pressure or O2 effects are unimportant then this needs to be detailed in the manuscript.

The carrier used was He in all photolysis experiments. We report results elsewhere (Gomez Martin et al, 2020) showing that iodine oxide clusters with even number of iodine atoms do not form, and that I_xO_y + H_2O reactions are extremely slow, either at low pressure or at higher pressures and with a more atmospherically representative matrix of gases. We have added this reference since this manuscript has very recently been accepted for publication in *Nat. Comm*.

Insertion in Page 12, Line 335: […], even for higher pressures and using N_2 as carrier gas (Gómez Martín et al., 2020)

Second, regarding more quantitative results, could photolysis quantum yields and therefore photolysis cross-sections differ as the pressure and identity of the surrounding gas matrix changes? Certainly these effects can be important for many atmospheric transients, not least for the actinometer NO2 though at a longer wavelength than used in this work. I suspect that such pressure effects will have a negligible impact on the quantitative results from this work, given, as stated on page 16, the featureless nature of the spectra. However, given the large divergence from atmospheric conditions noted above, a strong statement to the effect that these cross-sections / quantum yields are applicable to realistic atmospheric conditions would be advisable.

As the reviewer points out, NO_2 excitation at 355 nm is not dependent on the nature or pressure of the matrix, and is therefore suitable for use as an actinometer in these experiments (Troe, J. *Z. Phys. Chem*. 2000, **214**, p. 573-581). It is important to separate the two points being made here: firstly, the potential effect of the matrix on the chemistry leading to the formation of the molecules being studied in this work and secondly, the potential effect of the matrix on the photolysis quantum yield of the molecules being photolysed. Assuming the molecules are thermally equilibrated (a safe assumption at the pressures and timescales used in this study), the route to their formation has no bearing on the photolytic properties of the molecules. As the reviewer points out, the broad, featureless calculated absorption spectra indicate excitation to an unbound upper state. The photolysis processes in this study therefore do not depend on the nature and pressure of the matrix, and are suitable for use in atmospheric models.

Insertion in Page 9, Line 236: This is a reasonable assumption for broad band absorption spectra indicating excitation to an unbound upper state. The photolysis processes in this study therefore do not depend on the nature and pressure of the carrier gas matrix, and the results can be applied directly in atmospheric models.

Third regards the use of OIO as the actinometer for 532 nm experiments. I can understand why this molecule was used, given a limited set of alternatives. However, the manuscript needs to properly represent the problems that this introduces into the interpretation of results. The cross-section for OIO may be "relatively well known" as stated on page 8 (line 176), but I was not able to find a recent review justifying this statement. On the contrary, of the two references quoted in this work for OIO cross sections, only one (from Bloss et al.) quotes a value at 532 nm. A very quick look in the literature yielded cross-section data from five additional papers (Spietz 2005, Joseph 2005, Himmelmann 1996, Tucceri 2006 and from Ingham 2000) that differ by up to a factor of two at some wavelengths. Further, the quantum yield (QY) for atomic iodine production from OIO is certainly not established. Ingham et al. reported QY < 0.15 for this channel, in direct contrast to the value of unity taken from Gomez Martin et al. and used for the purposes of this work. Happily, a careful re-wording of the manuscript here can rectify these problems. First, the section on page 8 needs to take full account of the published literature on OIO. Second, the results obtained in this work need to be clearly denoted as being determined relative to the rather uncertain cross-sections and quantum yields for OIO at 532 nm.

Reviewer #1 has raised the same question. We have included in the revised manuscript a review of both the absorption cross section and the photolysis quantum yield of OIO at 532 nm. Note that Gomez Martin 2005 and Spietz et al. 2005 are part of the same body of work. While the former paper reported the cross section at a single wavelength and a higher resolution, the later reported the visible spectrum at a lower resolution. Overall, the four existing independent determinations do not deviate by more than ~25% from the average when they are extrapolated to 532 nm, and the relative cross sections measured by Bloss et al. and Spietz et al. across the visible spectrum are in very good agreement.

Insertion in Page 9, Line 225: The OIO absorption cross section at 532 nm is relatively well known, within 25% of the average value of the four independent determinations reported in the literature (Bloss et al., 2001; Joseph et al., 2005; Spietz et al., 2005; Tucceri et al., 2006). On the other hand, conflicting results have been reported for the OIO photolysis quantum yield (Tucceri et al., 2006; Gómez Martín et al., 2009). Here we use the unit quantum yield reported by Gomez Martin et al. (2009), which was determined in a system free of interferences from ozone where a long-lived I atom photofragment and no reformation of OIO was observed over a time scale of several milliseconds. This result is also supported by the short lifetime (200 fs) of the excited state responsible for the observed absorption bands (Ashworth et al., 2002) and the existence of a feasible photolysis path revealed by high level ab initio calculations (Peterson, 2010).

Lastly, on Figure 4 "an empirical fit" was used to obtain depletion parameters. What was the function? More interestingly, which processes were responsible for the delay in signal depletion following (presumably rapid) photolysis. Is this delay instrumental, and therefore present in other experiments? It is not possible for the reader to assess for themselves, as a very different timescale is presented on Figs 6 and 7.

This point has also been raised by Reviewer #1 and we have included a thorough explanation and a reference (Baeza-Romero et al., 2012) in the revised version of the manuscript.

More minor comments:

Page 2 it was stated that the main atmospheric fate of iodine atoms is reaction with O3 to form IO. This is likely true across much of the globe, but a significant alternative exists in polluted air (as encountered in many important areas of the coastal MBL) where reaction with NO2 to form INO2 would be competitive.
In an iodine-rich, semi-polluted environment like Roscoff (France), the NO_2 mixing ratios range between a few hundred ppt to a few ppb and the O_3 mixing ratios range from 10 to 50 ppb (Mahajan et al, 2009). Assuming the average mixing ratios registered in Roscoff during the RHaMBLe campaign, i.e. ~1 ppb NO_2 and ~30 ppb O_3, the ratio of first-order loss rates of atomic iodine to reaction with O_3 and NO_2 is ~7. Thus, it is a fair statement to say that the main atmospheric fate of atomic iodine is to react with ozone, even in semi-polluted, coastal environments.

The text on page 3 reports flows diluted in He whilst Figure 1 appears to indicate N2 as the principal diluent. Which is correct? If a mixture of the two then please use the text and / or the caption to Figure 1 to offer more detail.

Helium is correct. We have changed Figure 1 accordingly.

Similarly in the experimental details a laser energy of 120 mJ pulse-1 was reported. A more useful quantity for the reader would be the energy per pulse per square centimetre, as this more directly relates to absorption cross-sections (quoted in cm2 molecule) and consequent radical densities. Please supply this information / clarify.

Clarified in text to give the total laser energy per pulse and the laser energy per pulse per unit area (i.e. the laser pulse fluence).

The same applies to the YAG laser energy (page 5 line 116).

Clarified to give laser fluence (energy per pulse per unit area).

Technical: Page 3 line 63 – 65 was confusing.

Clarified. The CI-ToF-MS technique referred to uses a NO_3^- ion source. The observation of IO_3- signals is interpreted as a result of ambient HIO_3 being ionized by NO_3^-.

I think the authors mean to say "Since all reaction paths for I, IO or OIO with H2O are endothermic"

Changed.

Page 3 line 86 "introduced in the reactor" should be something like "introduced to the reactor"

Amended in text

The use of low-contrast colours on e.g. Fig 8 without other visual markers will make it very difficult for some readers to distinguish e.g. I2O2 from I2O3 from I2O4. Could dots or dashes be introduced to help with this issue of accessibility?

Done (now Figure 9)

Fig. 9 uses the same symbol type (circles) to represent I3O6, I3O7 and I5O12 – please make use of triangles / squares. Additionally, information was missing from the legend where only I5O12 is mentioned

Done (now Figure 10)

Paper Ref: acp-2020-456

Title: " Determination of the absorption cross-sections of higher order iodine oxides at 355 nm and 532 nm”

RESPONSE TO THE REPORT OF REVIEWER #3

We are grateful to the reviewer for helpful and constructive comments and suggestions. We address them point by point below. The Reviewer’s comments are shown in bold typescript, our response in normal typescript. Changes to the manuscript are highlighted in red. Page numbers refer to the revised manuscript.

The manuscript by Lewis et al. (acp-2020-456) describes experimental measurements and theoretical calculations to determine the absorption cross sections of higher iodine oxides, as well as modeling to assess the impact of the photochemistry in the atmosphere. The quality of the experimental data for what appear to be challenging experiments is reasonable. I have concerns that the modest theoretical methods applied may be inadequate to describe the electronically excited states in molecules such as the iodine oxides, but that is somewhat beyond my area of expertise. If the authors could demonstrate clearly that they are capable of reasonably predicting molecular properties of a well-known iodine oxide, it would go some way to assuaging those concerns.

Following the suggestion of the reviewer, we have compared the experimental absorption spectra of IO, OIO and HOI with the corresponding spectra calculated with the TD-DFT method. This comparison is shown in Figure A2 (below). It can be seen that even for radicals like IO and OIO, the method gives a reasonable prediction of the spectral position of the electronic bands, and average absorption cross sections of the same order. For closed-shell molecules, the agreement is expected to be better, as demonstrated for HOI.

We have introduced the following sentence in Page 10, at the end of section 2.2: Although there are more advanced methods for the calculation of electronic spectra, TD-DFT offers a reasonable compromise between low computational cost and accuracy of the predicted transitions. Figure A2 shows a comparison between the experimental and TD-DFT absorption spectra of IO, OIO and HOI. Note that although the TD-DFT method is not designed to predict ro-vibrational structure, the spectral positions of the electronic bands and the average absorption cross sections are in reasonable agreement with the experiment, even in the case of open shell species like IO and OIO. Higher iodine oxides are closed shell molecules and the accuracy of the transitions is expected to be similar to the result for HOI.

The new figure included in the Appendix A (Figure A2) is the following:

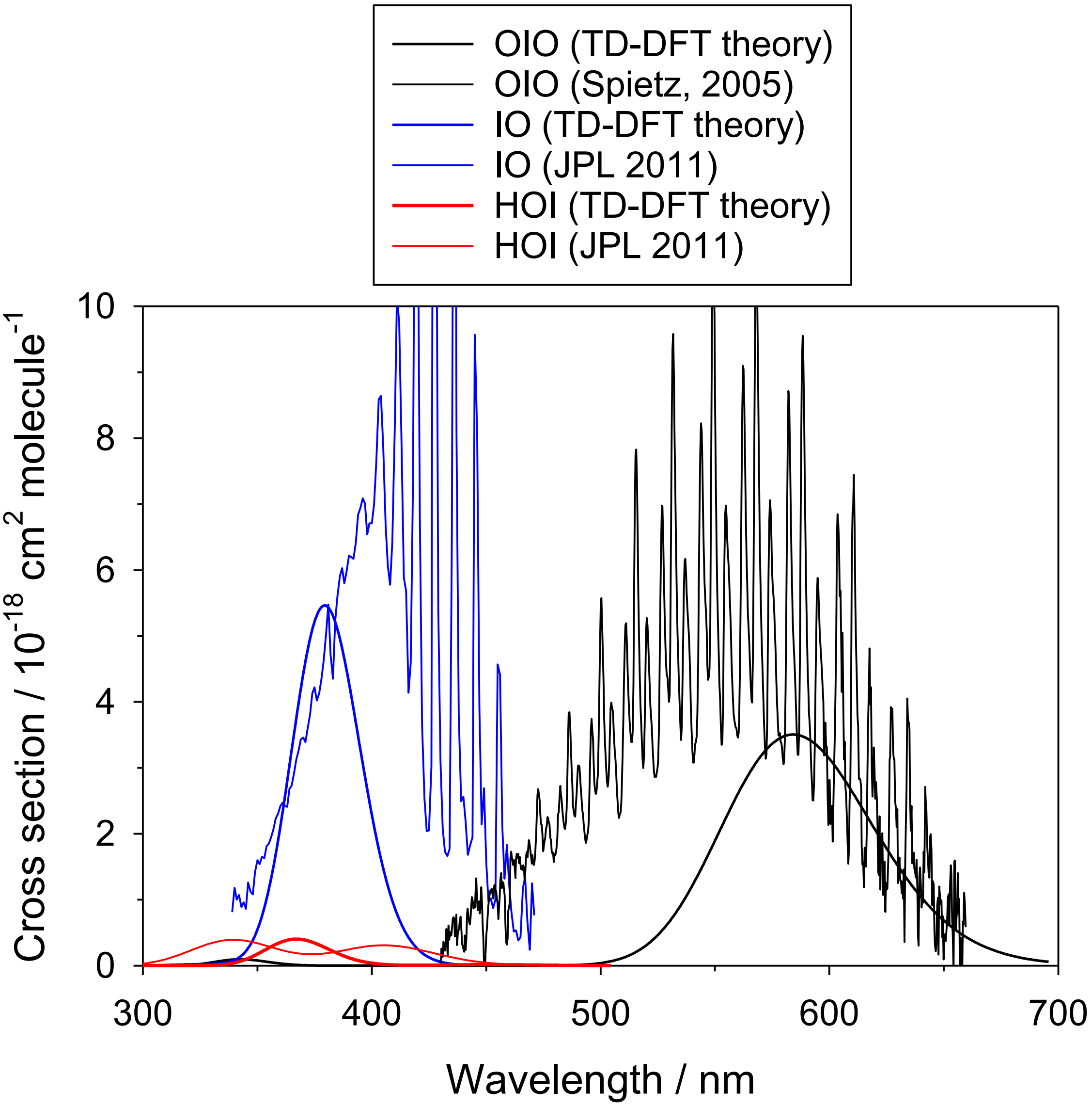

Figure A2: Experimental absorption cross sections of IO (Sander et al., 2011), OIO (Spietz et al., 2005) and HOI (Sander et al., 2011) and absorption spectra calculated with the TD-DFT method (this work).

I am unable to comment on the atmospheric modeling, although I would note that they rely on cross sections that have been determined experimentally at only two wavelengths.

Even though the experiments are limited to two wavelengths, this is significant progress with respect to what was known before. We use the two single-wavelength experimental cross sections to show that spectra measured by absorption spectroscopy cannot be directly used in the determination of photolysis rates and to validate calculated spectra, which do not suffer from absorption overlap issues. Of course, future studies should address experimentally the wavelength dependence of the absorption spectra of iodine oxides, e.g. by using the same approach presented in our work but with a tunable laser instead of a Nd:YAG laser.

The paper is, for the most part, fairly well-written although the structure could be improved. Some of the text in the methods section would be better located in the results section. For example, lines 144-179 (including Figure 3 and 4) describe measurements, not the experimental set-up, and belong in the results section, as do the results of the ab initio calculations.

This paper is not concerned with demonstrating the observation of I_xO_y by PI-ToF-MS, which has been already reported in previous publications. Since this method of detection of I_xO_y is already proven, we do not think that Figure 3 belongs to the results section, but rather to the methods section as a proof that we can see these species.

We have introduced the following sentence in Page 6, Line 137: Successful detection of I_xO_y by this method has been demonstrated elsewhere (Gomez Martin et al., 2013; Wei et al., 2017; Gomez Martin et al., 2020).

Similarly, Figure 4 and the corresponding discussion also deal with methodological considerations rather than with new results. The use of PI-TOF-MS in photochemical experiments has been discussed previously (Baeza-Romero et al, 2012). New text has been inserted in p. 8 after Figure 4 in response to another concern of the reviewers (see below), which further helps to appreciate the methodological nature of this section of the paper.

Regarding the ab initio calculations, we consider the determination of the ground state geometries and molecular parameters of iodine oxides as merely methodological, since there are previous publications where these have been reported at different levels of theory.

Insertion in p. 10, L245: Note that the ground states some of these oxides have been studied at a higher level of theory elsewhere (Kaltsoyannis and Plane, 2008; Galvez et al., 2013)

The novelty of these ab initio calculations is the determination of absorption spectra. We have added a new subsection 3.3 where the ab initio spectra are formally mentioned as results, and additional information about the spectra is provided.

Addition in Page 16:

3.3. Ab initio spectra

The calculated spectra are displayed in Figure 9 (I_2O_2, I_2O_3 and I_2O_4), Figure 10 (I_3O_6 and I_3O_7), and Figure 11 (IO_3). Oscillator strengths of the electronic transitions that are responsible for the visible and UV absorptions are provided in Appendix A. The TD-DFT spectra were wavelength-shifted by applying a constant energy shift to get agreement with the experiment at 355 nm. The shifts are quite modest, within the expected error at this level of theory (Foreman and Frisch 2015): I_2O_3 (30 kJ mol^{-1}), I_2O_4 (-12 kJ mol^{-1}), I_3O_6 (9.2 kJ mol^{-1}), I_3O_7 (-21 kJ mol^{-1}). Applying a constant energy shift means assuming that all the excited state energies are offset by a constant amount with respect to the ground state.

Table 1 compiles calculated geometries and vibrational frequencies, which are of little relevance to the subject matter of the paper and could be readily removed to supplementary information. On the other hand, no data for the calculated energies or oscillator strengths of the electronically excited states that are responsible for the visible and UV absorption are provided; the calculated ionization energy is also reported for only one species (IO3 on line 257). These data impact directly on the interpretation of the experimental results and should be compiled either in a revised version of Table 1 or in supplementary information.

Table 1 and Figure 5 have been removed from the main text and are now included in Appendix A following the reviewer request. The calculated oscillator strengths have been included in Appendix A as well.

Calculated and experimental ionization energies of I_xO_y species relevant to this work (except IO_3) have been reported previously, and the corresponding papers (Gómez Martín et al., 2013; Wei et al., 2017; Gómez Martín et al., 2020) are properly cited in the paper (page 6).

The results section would benefit from a clearer introduction to describe what IxOy species are detected in the experiment and their time dependence. A figure showing the different “kinetic profiles”, which are alluded to, would also be valuable. Presumably, the profiles have been characterized by varying the delay between the 248 nm photolysis pulse used to initiate the chemistry and the VUV photoionization pulse.

Why have clarified the species detected and the meaning of the “kinetic profiles” in the experimental section. Another wording for the same concept is “time trace”. The reviewer is correct in that time is defined as the delay between excimer photolysis and VUV photoionization.

Changes in Page 7, Lines 175-160: Each experiment results in a 3-dimensional dataset of signal intensity (proportional to concentration) vs. 248 nm photolysis - VUV photoionization delay time (kinetic profile or time trace) and time-of-flight (mass spectrum). Figure 3 shows mass spectra with the most prominent peaks obtained at different delay times . Mass-to-charge (m/z) calibration of time-of-flight was performed by selecting a number of well-known prominent mass peaks (e.g. IO at m/z =143, OIO at m/z =159, I2O3 at m/z =302, I2O4 at m/z =318 and I3O7 at m/z =493 (Gómez Martín et al., 2013)).

We now refer specifically to Figure 3 in the results section to make clearer what are the target species in the context of the mass spectrum. We have added a better introduction to the Results section, moving here some material from the Methods section describing how fragmentation problem affects our results and adding the requested figure with kinetic profiles:

As described in the experimental section, kinetic profiles of the growth and removal of the target iodine oxide species shown in Figure 3 were carried out in order to define the time periods with the most suitable kinetic profiles for photolysis measurements (Figure 5). Fragmentation of iodine oxides was a significant problem in these experiments, as predicted from ionization energy calculations of larger iodine oxides to possible photofragments at 10.5 eV (Gomez Martin et al., 2020). High amounts of active iodine (IO_x = I, IO) released from reaction R12 lead to fast formation of I_xO_y and particles. Under these conditions, at long times after the peak IO and OIO (~3-5 ms), the observed signal of IO, OIO and I_xO_y is contaminated by photofragmentation of higher order iodine oxides. For this reason, great care needed to be taken to establish a time window for each species wherein higher oxides are not present, to ensure that any depletion in the mass spectrometric signal for each species is exclusively due to the removal of the species via photolysis (Figure B1). Evidence of fragmentation comes in the form of a secondary growth in the signal seen for IO and OIO (Figure 5). The delay between the excimer and the Nd:YAG photolysis laser was therefore carefully selected to coincide with a period of relatively constant signal of the desired analyte, typically a maximum for short lived species, or a slow rise for larger reaction products of interest.

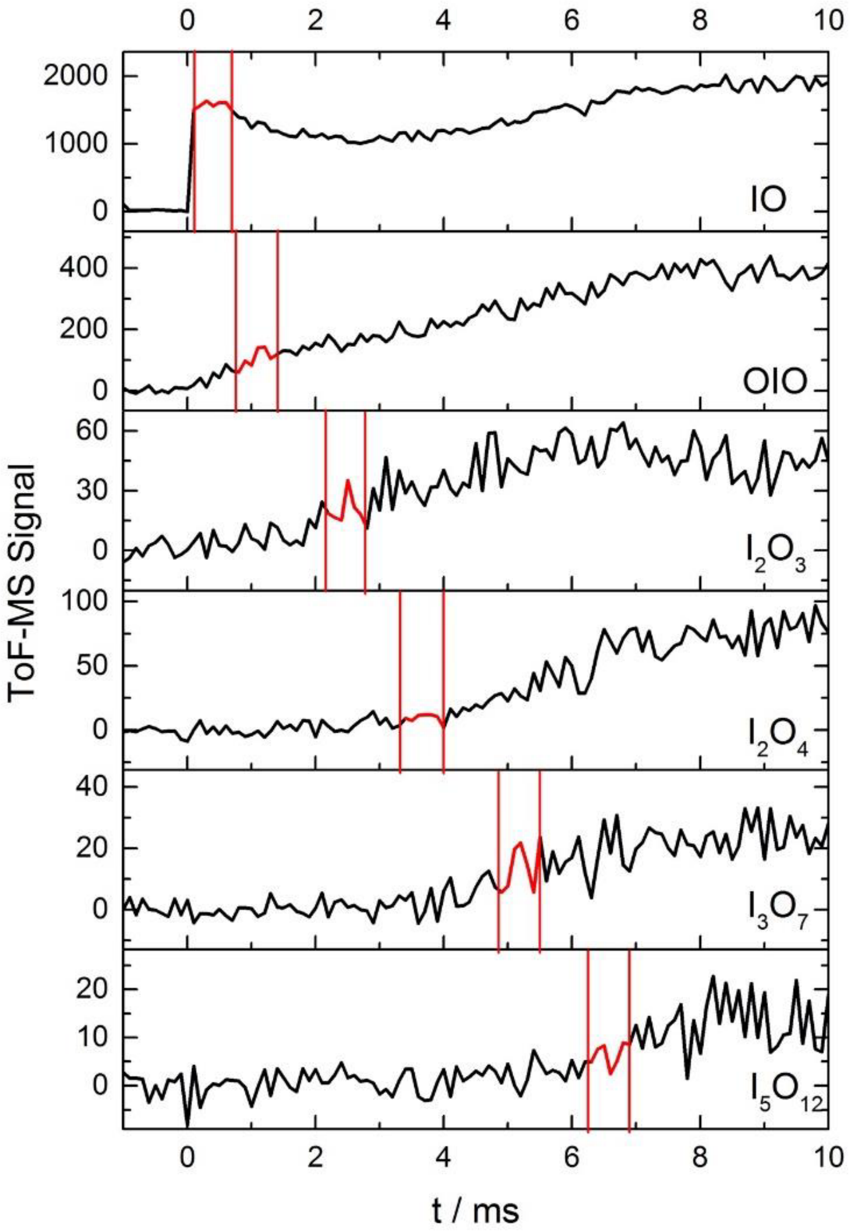

Figure 5: Time traces of IO, OIO, I_2O_3, I_2O_4, I_3O_7 and I_5O_{12} from -1-10 ms, at 1 ms intervals for a mixture of He (10 torr), O_3 and I_2 ($[O_3] = 4 \times 10^{14}$ molecule cm^{-2} $[I_2] = 2.8 \times 10^{14}$ molecule cm^{-2}) flash photolyzed by an excimer pulse at t = 0 (130 mJ $pulse^{-1}$). The red sections highlighted for each species correspond to the optimal delay windows for photolysis of the corresponding species for this set of conditions.

Kinetic profiles of IO, OIO, I_2O_3, I_2O_4, I_3O_7 and I_5O_{12} are shown in Figure 5, along with 0.5 ms windows within which each species can be photolysed free of contamination from daughter ions of larger I_xO_y species. To further illustrate the lack of contamination from higher oxides, the mass spectra collected during the windows outlined in the kinetic traces are averaged, showing the target species to be present absent of higher oxides (new Figure B1). The reviewer is correct to assume that contribution to a signal of interest from daughter ions of larger I_xO_y species would cause erroneous measurement of photodepletion in the species of interest, and as such, great care was taken to eliminate the possibility of the aforementioned contamination.

Note that the kinetic traces were obtained at the beginning of each experimental session, for each set of conditions, in order to elucidate the optimal time delay for a species of interest, whereby the signal was present, but not larger species, the daughter ions of which would contaminate the desired signal. The kinetic trace was generally not averaged for a long period of time, since good signal to noise is not required, and is just a preliminary check used to establish the correct timings for the photolysis experiments. This discussion appears now in Appendix B:

APENDIX B. Photofragmentation of I_xO_y species

The photofragmentation of I_xO_y species to daughter ions in the photoionization chamber of the detection apparatus necessitates careful experimentation in order to ensure that any photodepletion of a species of interest is solely due to its 355 nm or 532 nm photolysis in the flow tube, and not obscured by the daughter ions of larger I_xO_y species. To elucidate the optimal window for investigating photodepletion of each species, time resolved mass-spectra were recorded for each set of experimental conditions (Figure 5). From the kinetic information, it is then possible to inspect the averages of the mass spectra within these windows to ensure that the species of interest is present, but larger I_xO_y species are not, as shown in Figure B1. By ensuring no larger I_xO_y species are present, it follows that for a species of interest, only parent ions of the species are contributing to the signal intensity within that time window, and that no contribution to the recorded signal is coming from daughter ions. Note that the signals shown in Figure 5 and Figure B1 are not accumulated for extended periods of time, and as such are relatively noisy. Long accumulation times and corresponding large signal to noise ratios are unnecessary for these experiments, since the objective is simply to elucidate optimal time-delays within which photodepletion experiments are carried out, (photodepletion experiments are typically carried for ~10× as many accumulations) and are carried out prior to an experimental session. It should be noted also that the optimal timescales such as those shown in Figure 5 and Figure B1, vary depending on the concentration of IO formed at the beginning of the reaction sequence, and since the reactions which facilitate the stepwise formation of the higher oxides are second-order, even modest changes in [IO] at early times can result in significant changes to the appearance times of the different species of interest.

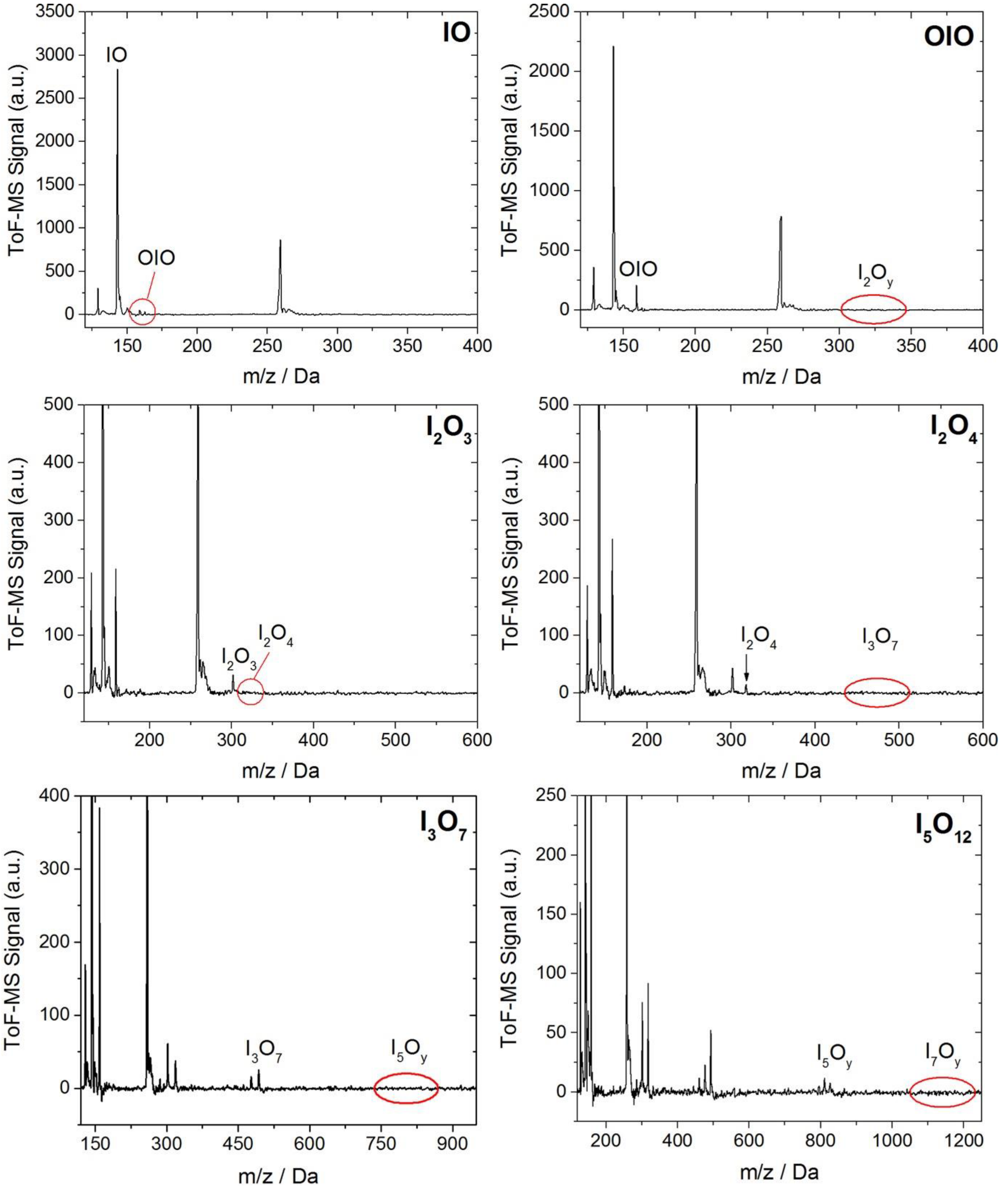

Figure B1: Mass spectra corresponding to the optimised time delays shown in Figure 5. The plots are generated by averaging the signal obtained for each mass over the 5 ms window. The species of interest is given in the top right corner of each spectrum.

The authors acknowledge (pages 13, 14) that fragmentation of larger species, can lead to signal increases at the masses of the photofragments, which would lead to possible systematic under-estimation of the depletion. To use the authors' example of I3O7, I have no sense of how much is present at the _7.6 ms time delay when the I2O4 (a potential daughter signal) is measured. Could other experimental parameters be varied (in

principle) to modify the relative yields of different IxOy species to explore this in more detail? Relative photoionization cross sections for the various species will also play a role.

This question is answered in conjunction with the previous question in the above response, and has been clarified with the aid of new figures in the main text and Appendix B.

The depletion measurements in Figure 6 and 7, as well as the NO2 depletion used for actinometry in Figure 4, are shown with an overlaid empirical fit. However, the fitting function is not described, or its choice explained, nor are any reasons for the different shapes discussed. Why does the effective "width" of the drop off appear to change for different species? Is it even meaningful? What delay does the time axis correspond to in these figures? The experiments use three laser pulses (two photolysis pulses, one to initiate the chemistry and a second to dissociate the iodine oxides) and one to detect the IxOy species. Clarity about which exactly which delay is being referred to would be helpful.

These points have been raised by Reviewers #1 and #2 as well. A detailed answer can be found in the response to Reviewer #1. We added the following piece of text to the manuscript to answer the reviewers' concerns:

Insertion in Page 8, Line 196: The trace shown in Figure 4, which is similar to all the traces obtained in this experiment, exhibits a delay between the pre- and post-photodepleted signal. This delay corresponds to an instrumental sampling time depending on the alignment of the lasers and the molecular masses of the bath gas and the sample species (Baeza-Romero et al., 2012). In the present experiments, it was necessary to leave a small gap (~2 mm) between the photolysis volume and the sampling pinhole, so as to avoid hitting the skimmer cone with the laser. The diffusional exchange of molecules between the photodepleted volume, and the un-photodepleted volume immediately before the pinhole blurs the onset of the photodepletion as it is measured by the TOF-MS. The values of S_0 and S_1 were obtaining by empirically fitting the photodepletion trace to a sigmoidal function:

$$y = S_0 + \frac{S_1 - S_0}{1 + 10^{(\log x_0 - x)p}} \tag{2}$$

Fitting to this function ensures that the flat sections corresponding to the pre- and post-photodepletion concentrations (S_0 and S_1 respectively) are characterized in the precise regions outside of the aforementioned "blurred" zone. The parameters x and p are not of scientific importance for this study and are simply instrumental factors.

Minor comments.

Figure 1. The photolysis laser arguably should be labeled also with 532 nm as some experiments use that wavelength.

Done

Line 113: Using the values for the cross section, concentration, and path length for I2 detection, I calculate OD = 0.82.

Apologies, 0.82 is correct, we mistakenly used the path length as 30 cm (the length of the Herriott cell) instead of 40 cm (the length of the single pass cell). This error is only in the specific example in the paper and the correct value of 40 cm was used in the work itself.

Figure 3. The caption could be more informative, for example, the time delay between the 248 nm pulse used to initiate the chemistry and the VUV photoionization pulse is not specified. Are the different colored traces the results of measurements at the optimum time for each?

The figure shows a complete time trace, averaged along the time axis, and is only intended to show a clear picture of the species being studied in this experiment, to give the reader an idea of how the peaks appear in the mass spectrum. The caption has been updated to clarify this fact.

Paper Ref: acp-2020-456

Title: " Determination of the absorption cross-sections of higher order iodine oxides at 355 nm and 532 nm”

RESPONSE TO THE REPORT OF REVIEWER #4

We are grateful to the reviewer for helpful and constructive comments and suggestions. We address them point by point below. The Reviewer’s comments are shown in bold typescript, our response in normal typescript. Changes to the manuscript are highlighted in red. Page numbers refer to the revised manuscript.

In this manuscript, Lewis et al. report experimental and theoretical determinations for the absorption cross-sections of iodine oxide species. Experimental measurements of the cross-sections were obtained using a technique that combined laser-flash photolysis (for production of iodine oxides from an I2/O3 mixture), photoionization mass spectrometry (for time-resolved species detection at 10.5 eV), and 355/532 nm laser photolysis. Cross-section measurements were calibrated using NO2 and OIO at 355 nm and 532 nm, respectively.

Theoretical determinations of the absorption spectra of the iodine oxides were obtained based on their B3LYP geometries. Atmospheric photolysis rates were determined across the actinic range using the theoretically-determined spectra, constrained by the experimental measurements, combined with the CAM-Chem model. In the experimental and results sections, the authors describe using the kinetic profiles of the iodine oxide species to determine at what delay times the second photolysis laser (355/532 nm) was fired for the absorption cross-section measurements. It would therefore be appropriate to present the complete time profiles of each of the species (in the absence of the second photolysis laser pulse) either in the main text or the supplementary information.

The same point has been raised by Reviewer #3. New Figure 5 includes some examples of full time traces as requested (the Figure is included in the response to Reviewer #3)

Please give the form of the function that is used to fit the photodepletion data in Figures 4, 6 and 7. There appears to be significant differences in the depletion behavior of the different species that the authors do not address. For example, why is the depletion of I2O4 much sharper than I3O7?

This point has been raised by Reviewers #1, #2 and #3, and has been clarified in the corresponding responses

What is the sensitivity of your measured cross-sections to the delay time of photolysis laser 2 (e.g. the 355 or 532 nm laser)?

The cross sections are insensitive to the delay time of the second photolysis laser, provided the species of interest is present, and uncontaminated by daughter ions of higher oxides. Great care was taken to assure that this was the case for all species being measured (see new Appendix B below).

What is the error in the theoretically determined absorption cross-sections? Does the magnitude of this error significantly impact the results of the atmospheric photolysis rates?

One thing we should have mentioned is that the TD-DFT spectra were wavelength shifted by applying a constant energy shift to get agreement with the experiment at 355 nm. The shifts are quite modest, within the expected error at this level of theory (Foreman and Frisch, 2015): I_2O_3 (30 kJ mol-1), I_2O_4 (-12 kJ mol-1), I_3O_6 (9.2 kJ mol^{-1}), I_3O_7 (-21 kJ mol^{-1}). Applying a constant energy shift means assuming that all the excited state energies are offset by a constant amount with respect to the ground state. As shown in Figure 10, the upper limits from experiment are within 20% of the theoretical calculations for linear I_3O_6 and I_3O_7.

Having anchored the theoretical absorption spectrum at 355 nm, we then assume that photolysis is possible up to the dissociation limit (which is the case for all the transitions of the I_xO_y ($x > 1$) molecules). A conservative estimate is a factor of 2 uncertainty in the J values for these molecules, which does not change the conclusions of our study.

We have introduced the following changes in the manuscript to clarify these points:

Page 16, first paragraph: The TD-DFT spectra were wavelength-shifted by applying a constant energy shift to get agreement with the experiment at 355 nm. The shifts are quite modest, within the expected error at this level of theory (Foreman and Frisch, 2015): I_2O_3 (30 kJ mol^{-1}), I_2O_4 (-12 kJ mol^{-1}), I_3O_6 (9.2 kJ mol^{-1}), I_3O_7 (-21 kJ mol^{-1}). Applying a constant energy shift means assuming that all the excited state energies are offset by a constant amount with respect to the ground state.

Page 17, Lines 407-409: The calculated spectra shown in Figure 9 and Figure 10 agree generally well with the experimentally determined values at 355 nm and 532 nm after small wavelength shifts indicated above. As shown in Figure 10, the upper limits from experiment are within 20% of the theoretical calculations for linear I_3O_6 and I_3O_7.

Page 20, Lines 463-465: Having anchored the theoretical absorption spectra at 355 nm, we then assume that photolysis is possible up to the dissociation limit (which is the case for all the transitions of the I_xO_y ($x > 1$) molecules). A conservative estimate is a factor of 2 uncertainty in the J values for these molecules.

There is very limited discussion about the potential impact of the daughter ions (referred to in the manuscript as photofragments) of larger iodine oxides on the determination of the cross-sections of smaller iodine oxides. Given that not all of the iodine oxides produced in the experiment have the same cross-section, if larger iodine oxides undergo dissociative ionization at 10.5 eV to photofragments with the same exact mass as the smaller iodine oxides studied in this work, the measured depletions of the smaller iodine oxide species would be perturbed by the contribution of photofragments from the larger iodine oxide species. To what extent do the authors have evidence that this is not significantly hampering their cross-section measurements?

The discussion about the impact of fragmentation has been expanded, including an Appendix B. Additional plots have been generated to illustrate the steps taken to eliminate this important potential effect highlighted by the reviewer (Figure B1). Essentially, kinetic profiles were taken for each set of conditions (new Figure 5), which allowed the optimal window for photolysis to be established, whereby the signal for a species is present in the spectrum, but any larger species which could photofragment to a daughter ion indistinguishable from the species of interest, is not present. In this way, it can be said with confidence, that daughter-ion contamination is not an issue in these experiments.

Addition to the manuscript:

APENDIX B. Photofragmentation of I_xO_y species

The photofragmentation of I_xO_y species to daughter ions in the photoionization chamber of the detection apparatus necessitates careful experimentation in order to ensure that any photodepletion of a species of interest is solely due to its 355 nm or 532 nm photolysis in the flow tube, and not obscured by the daughter ions of larger I_xO_y species. To elucidate the optimal window for investigating photodepletion of each species, time resolved mass-spectra were recorded for each set of experimental conditions (Figure 5). From the kinetic information, it is then possible to inspect the averages of the mass spectra within these windows to ensure that the species of interest is present, but larger I_xO_y species are not, as shown in Figure B1. By ensuring no larger I_xO_y species are present, it follows that for a species of interest, only parent ions of the species are contributing to the signal intensity within that time window, and that no contribution to the recorded signal is coming from daughter ions. Note that the signals shown in Figure 5 and Figure B1 are not accumulated for extended periods of time, and as such are relatively noisy. Long accumulation times and corresponding large signal to noise ratios are unnecessary for these experiments, since the objective is simply to elucidate optimal time-delays within which photodepletion experiments are carried out, (photodepletion experiments are typically carried for ~10× as many accumulations) and are carried out prior to an experimental session. It should be noted also that the optimal timescales such as those shown in Figure 5 and Figure B1, vary depending on the concentration of IO formed at the beginning of the reaction sequence, and since the reactions which facilitate the stepwise formation of the higher oxides are second-order, even modest changes in [IO] at early times can result in significant changes to the appearance times of the different species of interest.

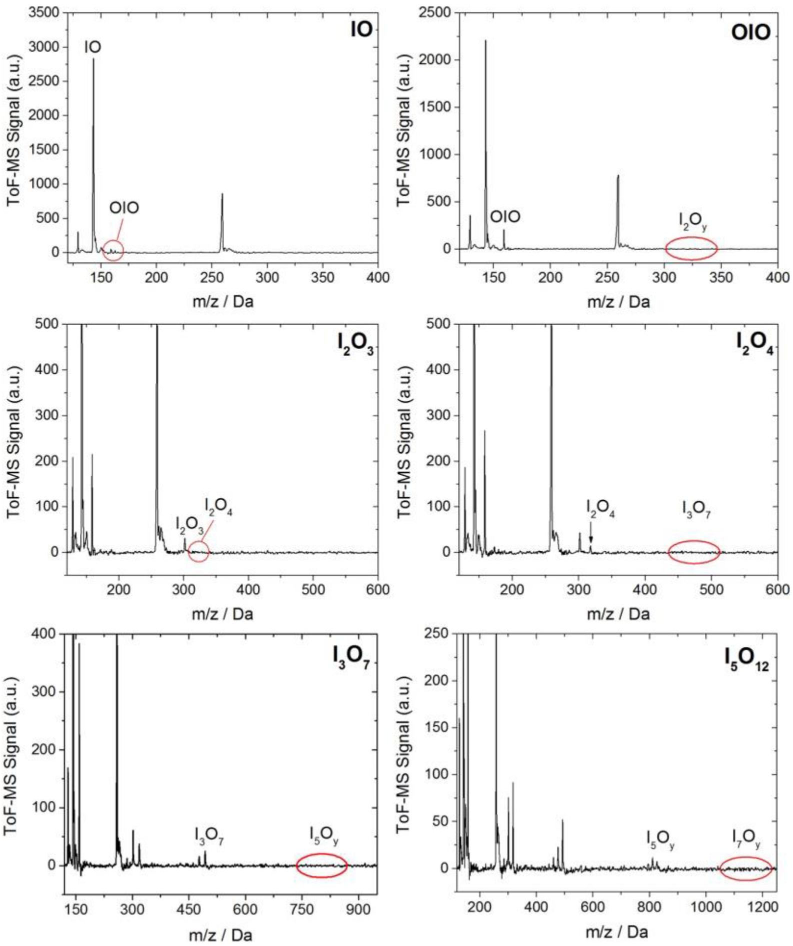

Figure B1: Mass spectra corresponding to the optimised time delays shown in Figure 5. The plots are generated by averaging the signal obtained for each mass over the 5 ms window. The species of interest is given in the top right corner of each spectrum.

Ionization energy calculations of larger iodine oxides to possible photofragments at the mass of the smaller iodine would indicate whether this is a concern or not at 10.5 eV.

Fragmentation is indeed a concern, as demonstrated by the traces of IO and OIO at longer delay times. Ab initio calculations of ionization and fragmentation energies are included in a recently accepted paper (Gomez Martin et al. 2020). We have included a reference in the paragraph introducing the results.

Additionally, measurements at reduced concentrations of [I], and at various delay times of the second photolysis laser would provide further indications of potential interference.

Appendix B explains the procedure for minimising the influence of daughter ions.

Minor comments: Figure 1 An entry port for H2O is indicated, is water used in any of these experiments?

Water was not used in these experiments. The Figure has been updated.

Section 2.1 For clarity, it would be helpful to distinguish the three laser pulses used in these experiments using a numbering scheme (e.g. photolysis pulse 1 or 2, photoionization pulse).

For clarity, the laser pulses have been amended in the text, and prefaced with either excimer, photolysis or PI laser.

Section 2.2 Table 1 and Figure 5 should be moved into the results section, or perhaps the supplementary information.

A new Appendix A has been added containing supplementary ab initio results.

L239 The number of significant figures in the value and the error for the I5O12 cross section are not consistent (and differ from the value in Table 2).

Amended in text

Determination of the absorption cross-sections of higher order iodine oxides at 355 nm and 532 nm.

Thomas R. Lewis[1,2], Juan Carlos Gómez Martín[3*], Mark A. Blitz[2], Carlos A. Cuevas[1], John M. C. Plane[2*] and Alfonso Saiz-Lopez[1*]

[1]Department of Atmospheric Chemistry and Climate, Institute of Physical Chemistry Rocasolano, CSIC, Madrid, Spain
[2]School of Chemistry, University of Leeds, LS29JT, Leeds, UK
[3]Instituto de Astrofísica de Andalucía, CSIC, 18008, Granada, Spain

**Correspondence to*: Juan Carlos Gómez Martín (jcgomez@iaa.es), John M. C. Plane (J.M.C.Plane@leeds.ac.uk) and Alfonso Saiz-López (a.saiz@csic.es).

Abstract. Iodine oxides (I_xO_y) play an important role in the atmospheric chemistry of iodine. They are initiators of new particle formation events in the coastal and polar boundary layer and act as iodine reservoirs in tropospheric ozone-depleting chemical cycles. Despite the importance of the aforementioned processes, the photochemistry of these molecules has not been studied in detail previously. Here, we report the first determination of the absorption cross sections of I_xO_y, x = 2, 3, 5, y = 1-12 at λ = 355 nm by combining pulsed laser photolysis of I_2/O_3 gas mixtures in air with time-resolved photo-ionization time-of-flight mass spectrometry, using NO_2 actinometry for signal calibration. The oxides selected for absorption cross section determinations are those presenting the strongest signals in the mass spectra, where signals containing 4 iodine atoms are absent. The method is validated by measuring the absorption cross section of IO at 355 nm, $\sigma_{355\ nm,\ IO} = (1.2 \pm 0.1) \times 10^{-18}$ cm^2, which is found to be in good agreement with the most recent literature. The results obtained are: $\sigma_{355\ nm,\ I2O3} < 5 \times 10^{-19}$ cm^2 molecule^{-1}, $\sigma_{355\ nm,\ I2O4} = (3.9 \pm 1.2) \times 10^{-18}$ cm^2 molecule^{-1}, $\sigma_{355\ nm,\ I3O6} = (6.1 \pm 1.6) \times 10^{-18}$ cm^2 molecule^{-1}, $\sigma_{355\ nm,\ I3O7} = (5.3 \pm 1.4) \times 10^{-18}$ cm^2 molecule^{-1} and , $\sigma_{355\ nm,\ I5O12} = (9.8 \pm 1.0) \times 10^{-18}$ cm^2 molecule^{-1}. Photodepletion at λ = 532 nm was only observed for OIO, which enabled determining upper limits for the absorption cross sections of I_xO_y at 532 nm using OIO as an actinometer. These measurements are supplemented with ab-initio calculations of electronic spectra in order to estimate atmospheric photolysis rates $J(I_xO_y)$. Our results confirm a high $J(I_xO_y)$ scenario where I_xO_y is efficiently removed during daytime, implying enhanced iodine-driven ozone depletion and hindering iodine particle formation. Possible I_2O_3 and I_2O_4 photolysis products are discussed, including IO_3, which may be a precursor to iodic acid (HIO_3) in the presence of HO_2.

1. Introduction

Photolabile iodine-containing molecules are emitted into the lower atmosphere from the sea surface and from marine biota. The atmospheric processing of iodine leads to its accumulation in aerosol, subsequent transport and deposition on land, where it enters the continental ecosystems (Saiz-Lopez et al., 2012b). In the course of this process, gas-phase reactive iodine is

Field Code Changed

involved in two important chemical processes of the background troposphere: ozone depletion and new particle formation . Iodine is thought to be responsible for 9 to 16% of the contemporary ozone removal in the tropical troposphere (Saiz-Lopez et al., 2014; Sherwen et al., 2016), and there is evidence that anthropogenic ozone pollution enhances iodine release from the sea surface (Carpenter et al., 2013; Chance et al., 2014; MacDonald et al., 2014; Prados-Roman et al., 2015; Cuevas et al., 2018), which in turn has accelerated ozone loss in the last decades (Cuevas et al., 2018). The atmospheric chemistry of iodine is in principle fairly simple, since the main atmospheric fate of the iodine atoms is reaction with ozone to form iodine monoxide (IO). This radical photolyzes readily (Gómez Martín et al., 2005), creating an ozone-neutral cycle and establishing a steady state concentration of I and IO, which are then termed collectively as active iodine or IO_x. Any other chemical cycle involving IO which recycles atomic iodine without concomitant generation of atomic oxygen leads to ozone depletion, e.g. (Gómez Martín et al., 2009):

$$I + O_3 \rightarrow IO + O_2 \qquad (R1)$$

$$IO + IO \rightarrow OIO + I \qquad (R2)$$

$$\underline{OIO + h\nu \rightarrow I + O_2} \qquad (R3)$$

$$\text{Net: } 2O_3 \rightarrow 3O_2$$

Further steps in this scheme lead to the formation of higher iodine oxides (Gómez Martín et al., 2013):

$$IO + IO \rightarrow I_2O_2 \qquad (R4)$$

$$IO + OIO \rightarrow I_2O_3 \qquad (R5)$$

$$OIO + OIO \rightarrow I_2O_4 \qquad (R6)$$

$$I_xO_y + I_xO_y \rightarrow\rightarrow\rightarrow \text{particles} \qquad (R7)$$

Previous laboratory experiments on iodine photochemistry have reported kinetic growth of broad band absorptions following the decay of IO and OIO as well as significant deposition of particulates on the walls of the reactors (Cox and Coker, 1983; Laszlo et al., 1995; Harwood et al., 1997; Gómez Martín et al., 2005). These broad band absorbers have been tentatively identified as some of the higher iodine oxides produced in reactions R4, R5 and R6 (Bloss et al., 2001; Gómez Martín et al., 2007), which are believed to be precursors to the particles that eventually deposit on the walls. Furthermore, iodine oxide containing particles have been observed in multiple aerosol flow tube and steady state chamber experiments starting from the photooxidation of iodine precursors directly injected into the chamber (Hoffmann et al., 2001; Jimenez et al., 2003; Saunders et al., 2010; Wei et al., 2017) or emitted from cultures of algae under oxidative stress (McFiggans et al., 2004; Pirjola et al., 2005). Emissions of I_2 and alkyl-iodides from coastal macroalgae and polar phytoplankton and concurrent observation of IO and OIO (Saiz-Lopez and Plane, 2004) have been unambiguously linked to intense new particle formation events (Jimenez et al., 2003; McFiggans et al., 2004). Thus, there is a strong indication that iodine oxide clustering also happens in the coastal boundary layer and is responsible for particle formation events.

Recent Nitrate Ion Chemical Ionization - Atmospheric Pressure Interface- Time of Flight Mass Spectrometry (NO_3^- CI-API-ToF-MS) observations of IO_3^- and IO_3-containing ion clusters in coastal and polar environments, as well as complementary laboratory experiments in the absence of HO_x, have been interpreted as direct measurements of gas-phase iodic acid ($HOIO_2$, hereafter denoted as HIO_3) and HIO_3 clusters (Sipilä et al., 2016) by ionization of the ambient species by NO_3^- in the instrument inlet. Since all possible reaction paths for I, IO and OIO with H_2O are very endothermic (Canneaux et al., 2010; Hammaecher et al., 2011; Khanniche et al., 2017a), and IO_x–H_2O complexes are very weakly bound (Galvez et al., 2013), the formation of oxyacids may rather proceed via hydrolysis of higher iodine oxides (Kumar et al., 2018):

Field Code Changed

Deleted: between

Deleted: and I, IO and OIO

Field Code Changed

Field Code Changed

Field Code Changed

Field Code Changed

Field Code Changed

$$I_2O_y + H_2O \rightarrow HIO_x + HIO_{y-x+1} \qquad \text{(R8)}$$

Ozone depletion and particle formation are to some extent competing processes. Significant I_xO_y photolysis rates may result in regeneration of IO_x:

$$I_2O_2 + h\nu \rightarrow IO + IO \qquad \text{(R9a)}$$

$$\rightarrow I + OIO \qquad \text{(R9b)}$$

$$I_2O_3 + h\nu \rightarrow IO + OIO \qquad \text{(R10a)}$$

$$\rightarrow I + IO_3 \qquad \text{(R10b)}$$

$$I_2O_4 + h\nu \rightarrow OIO + OIO \qquad \text{(R11a)}$$

$$\rightarrow IO + IO_3 \qquad \text{(R11b)}$$

These photochemical reactions would enhance ozone depletion, while slowing down the incorporation of iodine into aerosol via oxides and/or oxyacids, and represent an important source of uncertainty in the iodine chemical mechanism incorporated into global chemistry transport models (Saiz-Lopez et al., 2014; Sherwen et al., 2016). In order to reduce this uncertainty, we report here a set of I_xO_y photodepletion experiments with mass spectrometric detection, which enables unambiguous observation of all the species of interest (Gómez Martín et al., 2013). Experiments devoted to understanding the interaction between I_xO_y and water, potentially leading to the formation of HIO_3, will be reported elsewhere.

Deleted: . This is currently

Field Code Changed

Field Code Changed

Field Code Changed

2. Methods

2.1. Experimental set-up

A pulsed laser photolysis (PLP) system has been employed to generate iodine oxides from the photolysis of O_3 in the presence of I_2 in a tubular reaction cell (Figure 1). A flow of typically 1.5 slm of He carrier gas (99.999%, BOC Gases) was introduced in the reactor. I_2 molecules were entrained in the carrier flow by passing a smaller flow of He (~100 sccm) through a 12 mm diameter temperature-stabilized Teflon tube containing I_2 crystals (>99.5%, Sigma-Aldrich). An electrical discharge ozone generator converted ~2% of a ~100 sccm O_2 flow (99.999%, BOC Gases) to O_3, which was introduced to the main flow via an inlet on the flow tube.

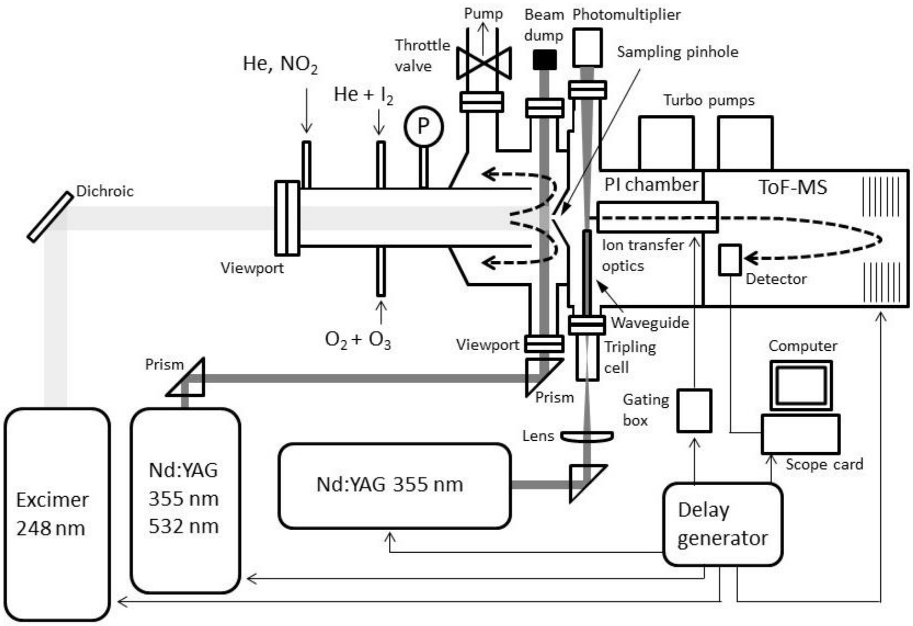

Figure 1: Schematic diagram of the experimental set-up for studying the photolysis of iodine oxides

Ozone was photolyzed at 248 nm by an excimer laser beam (Lambda Physik Compex 102), which was passed unfocussed through a quartz viewport along the tube main axis. This generated the well-known sequence of reactions:

$O_3 + hv \rightarrow O(^1D) + O_2$ (R12)

$O(^1D) + M \rightarrow O(^3P) + M$ (R13)

$O(^3P) + I_2 \rightarrow IO + I$ (R14)

followed by reactions R1, R2, R4, R5 and R6, as well as further I_xO_y clustering reactions. The precursor concentrations ($[I_2]$~ 2-4 × 10^{14} molecule cm^{-3}, $[O_3]$~ 3-5 × 10^{14} molecule cm^{-3}) and excimer laser energy (120-190 mJ $pulse^{-1}$, ~50-80 mJ $pulse^{-1}$ cm^{-2}) were tuned to ensure that I_2 was in excess over $O(^3P)$. Iodine and ozone concentrations were measured using a 532 nm solid state laser in a single pass and a multipass Herriot cell (Lewis et al., 2018), respectively (Figure 2). A reflection (~5%)

Deleted: (

Deleted:)

Deleted:)

Field Code Changed

of the main 532 nm diode laser (Thorlabs CPS532 532 nm 4.5 mW) beam was directed along the length of the cell (length = 40 cm) and detected using a photodiode detector (Thorlabs SM05PD3A). Ozone was detected by passing the main beam through a hole in the rear of a silver-coated concave mirror (Thorlabs CM508-200-P01 f = 20 cm) onto an identical mirror (without a hole) positioned 40 cm from the first mirror. The light was passed 40 times through the cell, and exits through the same entrance hole (some passes are omitted from the diagram for simplicity), giving a path length of 12 m.

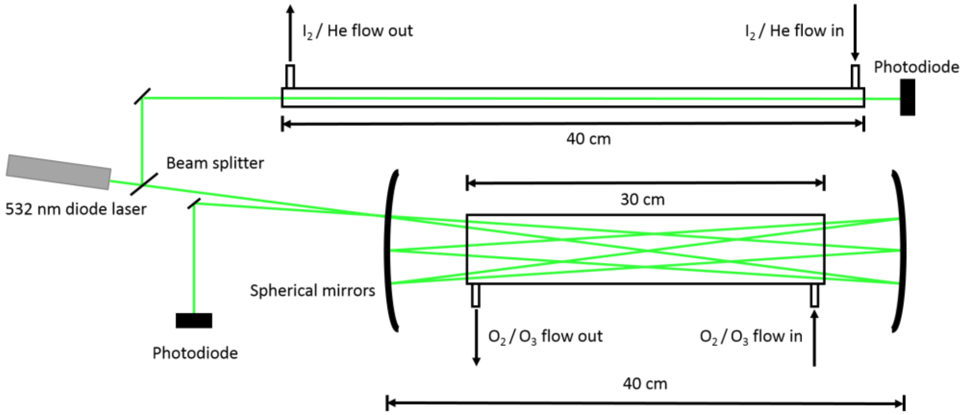

Figure 2: A Schematic of the absorption setup used to measure both I_2 and O_3

The concentrations C of O_3 and I_2 were then determined using the Beer-Lambert law (equation 1), where I and I_0 are the intensities of the 532 nm laser light recorded with and without the reagent present, respectively, OD is the optical density, σ the absorption cross section, and l the optical path length:

$$OD = \ln\frac{I_0}{I} = \sigma \cdot C \cdot l \qquad (1)$$

O_3 has an absorption cross-section at 532 nm of 2.34×10^{-21} cm^2 molecule^{-1} (Burrows et al., 1999). A typical concentration of 5×10^{14} molecule cm^{-3} in the reaction mixture (total flow ~1700 sccm) requires a concentration in the O_3/O_2 flow (100 sccm) of around 8.5×10^{15} molecule cm^{-3}. An ozone concentration of 8.5×10^{15} molecule cm^{-3} results in $OD = 0.024$. I_2 has an absorption cross-section at 532 nm of 3.03×10^{-18} cm^2 molecule^{-1}(Saiz-Lopez et al., 2004). A typical I_2 concentration of 4×10^{14} molecule cm^{-3} in the reaction mixture (total flow ~1700 sccm) requires a concentration in the I_2/He flow (100 sccm) of around 6.8×10^{15} molecule cm^{-3}. An I_2 concentration of 6.8×10^{15} molecule cm^{-3}, giving $OD = 0.82$. The ODs observed for both species are easily detectable by the instrument, which has a typical signal-to-noise ratio of ~ 400 , which corresponds to a minimum detectable OD of 2.5×10^{-3}. As there is no reference photodiode in this setup, drift in laser intensity must be accounted for. To negate the effect of laser drift as much as possible, the probe intensity is measured over a period of 15 seconds for both I and I_0, with ~10s between the measurements. To ensure that laser drift does not significantly affect the

Field Code Changed

Field Code Changed

Deleted: 6

Deleted: is

Deleted: ing

measured concentrations, measurements are taken until 3 concordant results are obtained (typically the first three results).

In order to measure the photodepletion of the I_xO_y molecules at 532 nm and 355 nm, a frequency-doubled or tripled Nd:YAG laser beam (Continuum Surelite 10-II, 1 cm^{-1} linewidth, 20 ns pulse width, ~80 mJ $pulse^{-1}$ cm^{-2} at 532 nm and ~50 mJ $pulse^{-1}$ cm^{-2} at 355 nm) was passed across the flow tube, perpendicular to the main axis and near the sampling point. Experiments were carried out at 4-7 Torr. The pressure in the reactor was set by a throttle valve placed upstream of an Edwards 80 roots blower – oil rotary pump combination. The flows were set using MKS calibrated mass flow controllers and pressure was measured using a set of 10 Torr and 1000 Torr MKS Baratron pressure transducers.

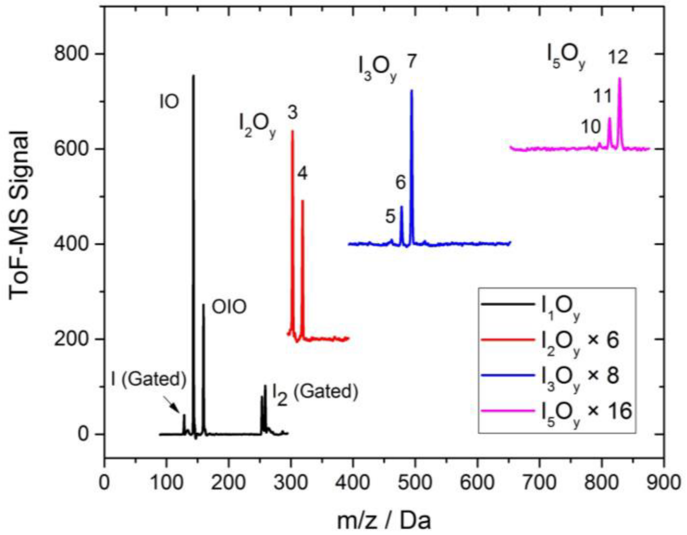

Figure 3: Mass spectra in four different m/z ranges encompassing peaks of species with 1, 2, 3 and 5 iodine atoms. Some of the spectra are scaled and shifted for clarity. The mass-spectra are generated by averaging the mass spectra at each time point, over a 20 ms experiment comprising 20 individual time points.

The iodine oxides generated were sampled in situ from the irradiated volume through a pinhole (200 μm diameter) situated on axis into a Kore Technology photo-ionization time-of-flight mass spectrometer (PI-ToF-MS) described in detail elsewhere (Gómez Martín et al., 2016). Successful detection of I_xO_y by this method has been demonstrated elsewhere (Gómez Martín et al., 2013; Wei et al., 2017; Gómez Martín et al., 2020). The PI chamber of this instrument (~10^{-4} Torr) is fitted with viewports, allowing a pulsed laser beam to be directed through the high density region of the sampled gas jet. Iodine oxides have ionization potentials in the range of 9-11 eV (Gómez Martín et al., 2013; Wei et al., 2017), which requires generating a vacuum ultraviolet (VUV) laser ionization beam. This is achieved by tightly focusing the 355 nm output of a frequency-tripled Nd:YAG laser (Continuum Surelite 10-II pulse width 3-5 ns) in a cell filled with xenon, which produces VUV radiation by frequency tripling

Deleted: .

Field Code Changed

Field Code Changed

Field Code Changed

(118 nm , or equivalently 10.5 eV) (Kung et al., 1973; Mahon et al., 1979). The resulting positive ions are accelerated towards the ToF-MS by means of a continuous negative voltage. An electron photomultiplier detector coupled to a pre-amplifier outputs an analog signal, which is registered by the digital oscilloscope (Picoscope 6000). A limitation of this method is that large signals (e.g. I_2^+ and I^+) cause detector overload during a significant time span after the large peak has been registered. An analog gating box is used to lessen these effects by sending a (~ 400 ns wide) gating pulse to the ion extraction optics. Gating in this way removed >90% of the overloaded signal from I_2^+ and I^+, significantly improving the signal to overload ratio.

Field Code Changed

Field Code Changed

Synchronization between the chemistry-initiating excimer laser pulse, the photolysis laser, the probing PI laser pulse and the detection devices is provided by a computer-controlled delay generator (Quantum Composers, 9518). In this manner, the delay between PLP and PI can be varied in order to observe the kinetics of reactants and products, and the photodepletion of the species of interest. The experiment repetition rate was set at 10 Hz, the optimal repetition rate for operation of both the VUV generating PI YAG laser and the YAG laser used for photolysis of the iodine oxides. A LabView program built in-house provides a sequence of delays between the PLP and PI lasers which can be modified by the user via a graphical interface. Desired experimental parameters are input into the LabView program, including the number of pre-photolysis points, the number of experimental data, the duration of the experiment and the number of repetitions. Each experiment results in a 3-dimensional dataset of signal intensity (proportional to concentration) vs. 248 nm photolysis - VUV photoionization delay time (kinetic profile or time trace) and time-of-flight (mass spectrum). Figure 3 shows mass spectra with the most prominent peaks obtained at different delay times. Mass-to-charge (*m/z*) calibration of time-of-flight was performed by selecting a number of well-known prominent mass peaks (e.g. IO at *m/z* =143, OIO at *m/z* =159, I_2O_3 at *m/z* =302, I_2O_4 at *m/z* =318 and I_3O_7 at *m/z* =493 (Gómez Martín et al., 2013)).

Field Code Changed

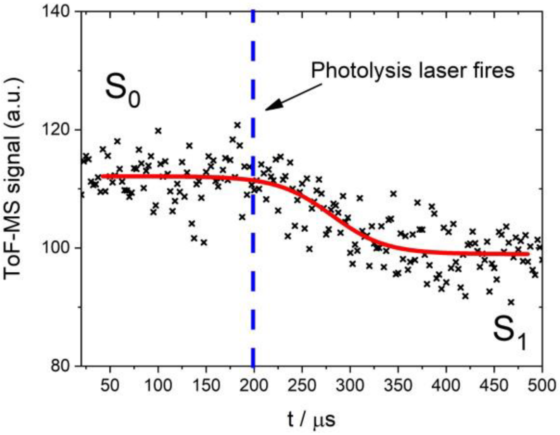

Figure 4: Schematic of a photodepletion measurement of NO_2. The red curve is an empirical fit through the data performed to obtain the values of S_0 and S_1.

To investigate the photodepletion of I_xO_y, it is desirable to keep the signal of the species of interest relatively constant over the delay window used to probe the photolysis. The timing of the Nd:YAG photolysis laser pulse was programmed to a fixed delay with respect to the 248 nm excimer pulse. To find the optimal window in which to conduct photolysis experiments, the reaction kinetics were first explored between 0 and ~10 ms for different sets of conditions. It was important to generate a sufficiently high concentration of I_xO_y to obtain a good signal-to-noise ratio, but not so high that the growth/removal timescale was comparable to the observed photodepletion (~400 µs).

The trace shown in Figure 4, which is similar to all the traces obtained in this experiment, exhibits a delay between the pre- and post-photodepleted signal. This delay corresponds to an instrumental sampling time depending on the alignment of the lasers and the molecular masses of the bath gas and the sample species (Baeza-Romero et al., 2012). In the present experiments, it was necessary to leave a small gap (~2 mm) between the photolysis volume and the sampling pinhole, so as to avoid hitting the skimmer cone with the laser. The diffusional exchange of molecules between the photodepleted volume, and the un-photodepleted volume immediately before the pinhole blurs the onset of the photodepletion as it is measured by the TOF-MS. The values of S_0 and S_1 were obtaining by empirically fitting the photodepletion trace to a sigmoidal function:

$$y = S_0 + \frac{S_1 - S_0}{1 + 10^{(\log x_0 - x)p}} \qquad (2)$$

Fitting to this function ensures that the flat sections corresponding to the pre- and post-photodepletion concentrations (S_0 and S_1 respectively) are characterized in the precise regions outside of the aforementioned "blurred" zone. The parameters *x* and *p* are not of scientific importance for this study and are simply instrumental factors.

The photolysis laser depletes any analyte within the photolysis volume which exhibits a bound-unbound transition at the energy of the photolysis wavelength used for each experiment. The signals for a certain *m/z* ratio before and after the photolysis laser is fired are respectively noted as S_0 and S_1 (Figure 4). Absorption cross sections were then calculated by comparing the relative signal change (ζ_{IxOy}) for the analyte of interest to the relative signal change (ζ_{REF}) for a molecule having a well-studied spectrum in an analogous actinometric experiment using the same configuration and laser fluence. In this way, systematic errors arising from the beam energy and area are eliminated in the determination of the actinic flux *F*:

$$\frac{S_{REF\,0} - S_{REF}}{S_{REF\,0}} = \frac{[X_{REF}]_0 - [X_{REF}]}{[X_{REF}]_0} \equiv \zeta_{REF} = 1 - e^{-F \cdot \sigma_{X_{REF}} \cdot \phi_{X_{REF}}} \qquad (3)$$

$$F = -\frac{1}{\sigma_{X_{REF}} \cdot \phi_{X_{REF}}} \ln(1 - \zeta_{REF}) \qquad (4)$$

Similarly, for the target I_xO_y molecule we have:

$$\frac{S_{IxOy\,0} - S_{IxOy}}{S_{IxOy\,0}} = \frac{[I_xO_y]_0 - [I_xO_y]}{[I_xO_y]_0} \equiv \zeta_{I_xO_y} = 1 - e^{-F \cdot \sigma_{I_xO_y} \cdot \phi_{I_xO_y}} \qquad (5)$$

$$\sigma_{I_xO_y} \cdot \phi_{I_xO_y} = -\frac{1}{F} \ln(1 - \zeta_{I_xO_y}) \qquad (6)$$

Inserting equation 4 in equation 6, we have:

Deleted: shot

Deleted: flash

Deleted: similarly

Field Code Changed

Deleted:

Moved down [2]: Fragmentation of iodine oxides was a significant problem in these experiments where the amount of active iodine (IO_x = I, IO) released from reaction R12 is high, leading to fast formation of I_xO_y and particles. Under these conditions, at long times after the peak IO and OIO (~3-5 ms), the observed signal of IO, OIO and I_xO_y is contaminated by photofragmentation of higher order iodine oxides. For this reason, great care needed to be taken to establish a time window for each species wherein higher oxides are not present, to ensure that any depletion in the mass spectrometric signal for each species is exclusively due to the removal of the species via photolysis. Evidence of fragmentation comes in the form of a secondary growth in the signal seen for IO and OIO. The delay between the excimer and the Nd:YAG photolysis laser was therefore carefully selected to coincide with a period of relatively constant signal of the desired analyte, typically a maximum for short lived species, or a slow rise for larger reaction products of interest.¶

Deleted: 2

Deleted: 3

Deleted: 4

Deleted: 5

Deleted: 3

Deleted: 5

$$\sigma_{I_xO_y}\cdot\phi_{I_xO_y}=\sigma_{X_{REF}}\phi_{X_{REF}}\frac{\ln(1-\zeta_{I_xO_y})}{\ln(1-\zeta_{REF})} \qquad (7)$$

NO_2 (99.5%, BDH, 10% in He) was the best reference molecule to perform actinometry at 355 nm. In this case, $\sigma_{X_{REF}} = \sigma_{NO_2(355\,nm)} = 5.3 \times 10^{-19}$ cm^2 molecule^{-1} (Vandaele et al., 1998) and $\phi_{X_{REF}} = \phi_{NO_2(355\,nm)} = 1$ (Burkholder et al., 2015). Typically, NO_2 depletion was around 8% in the actinometric experiments. For the 532 nm photolysis experiments, OIO was chosen as reference, owing to the low sensitivity of its broad absorption bands to photolysis laser resolution, as opposed, for example, to I_2. The use of I_2 as actinometer is also precluded by the overload issue mentioned above. The OIO absorption cross section at 532 nm is relatively well known, within 25% of the average value of the four independent determinations reported in the literature (Bloss et al., 2001; Joseph et al., 2005; Spietz et al., 2005; Tucceri et al., 2006). On the other hand, conflicting results have been reported for the OIO photolysis quantum yield (Tucceri et al., 2006; Gómez Martín et al., 2009). Here we use the unit quantum yield reported by Gomez Martin et al. (2009), which was determined in a system free of interferences from ozone where a long-lived I atom photofragment and no reformation of OIO was observed over a time scale of several milliseconds. This result is also supported by the short lifetime (200 fs) of the excited state responsible for the observed absorption bands (Ashworth et al., 2002) and the existence of a feasible photolysis path revealed by high level ab initio calculations (Peterson, 2010). Thus $\sigma_{X_{REF}} = \sigma_{OIO(532\,nm)} = 9.5 \times 10^{-18}$ cm^2 molecule^{-1} (Bloss et al., 2001; Spietz et al., 2005) and $\phi_{X_{REF}} = \phi_{OIO(532\,nm)} = 1$ (Gómez Martín et al., 2009). In principle, equation 7 yields the photolysis cross section, i.e. the product $\sigma_{I_xO_y}\cdot\phi_{I_xO_y}$, which is equal to the absorption cross section if $\phi_{I_xO_y} = 1$. This is a reasonable assumption for broad band absorption spectra indicating excitation to an unbound upper state. The photolysis processes in this study therefore do not depend on the nature and pressure of the carrier gas matrix, and the results can be applied directly in atmospheric models.

2.2. Ab initio calculations

The geometry of the ground electronic state of IO_3, I_2O_3, I_2O_4, I_3O_6 and I_3O_7 was optimized by using the B3LYP functional combined with the standard 6-311+G(2d,p) triple-ζ basis set for O and H, and an all-electron (AE) basis set for I (Glukhovtsev et al., 1995). The AE basis set is a contracted (15s12p6d)/[10s9p4d] 6-311G basis, the [5211111111,411111111,3111] contraction scheme supplemented by diffuse s and p functions, together with d and f polarization functions. See Glukhovtsev et al. (1995) for further details. Figure A1 illustrates the geometries of the various iodine oxides and hydroxy- species that are discussed in Section 4. The corresponding molecular parameters (Cartesian coordinates, rotational constants and vibrational frequencies) are listed in Table A1. Note that the ground states some of these oxides have been studied at a higher level of theory elsewhere (Kaltsoyannis and Plane, 2008; Galvez et al., 2013).

The absorption cross-sections of the aforementioned molecules were calculated using the time-dependent density functional (TD-DFT) excited states method (Stratmann et al., 1998) within the Gaussian 16 suite of programs (Frisch et al., 2016). The vertical excitation frequencies ($\tilde{\nu}_i$) and oscillator strengths (f_i) were obtained for the first 30 excited states (Table S2). The

Deleted: 6

Field Code Changed

Field Code Changed

Deleted: (

Deleted:)

Deleted: and

Deleted: absorption cross sections

Field Code Changed

Field Code Changed

Field Code Changed

Field Code Changed

Moved down [1]: (Bloss et al., 2001; Gómez Martín et al., 2005).

Field Code Changed

Field Code Changed

Field Code Changed

Field Code Changed

Field Code Changed

Deleted:

Field Code Changed

Field Code Changed

Moved (insertion) [1]

Deleted: (Bloss et al., 2001; Gómez Martín et al., 2005)

Field Code Changed

Deleted: 6

Deleted: .

Field Code Changed

Field Code Changed

Deleted: 5

Field Code Changed

Field Code Changed

Deleted: Table 1: Molecular properties of I_2O_3, I_2O_4, I_3O_6 (cyclic), I_3O_6 (linear), I_3O_7 (cyclic), I_3O_7 (linear), IO_3 and the transition state for dissociation of IO_3 to IO + O_2 ...

Field Code Changed

Field Code Changed

cross section $\sigma(\tilde{\nu})$ at frequency $\tilde{\nu}$ was then computed using the GaussView program (Dennington et al., 2016):

$$\sigma(\tilde{\nu}) = 2.17 \times 10^{-16} \quad \sum_{i=1}^{n}\left(\frac{f_i}{\Delta}\exp\left[-\left(\frac{\tilde{\nu}-\tilde{\nu}_i}{\Delta}\right)^2\right]\right) \qquad (8)$$

where the summation is over the 30 electronic excited states and $\sigma(\tilde{\nu})$ is in units of cm^2 $molecule^{-1}$. Each peak is assumed to have a Gaussian band shape with a width Δ, set here to the default value (Dennington et al., 2016) of 0.4 eV. Although there are more advanced methods for the calculation of electronic spectra, TD-DFT offers a reasonable compromise between low computational cost and accuracy of the predicted transitions. Figure A2 shows a comparison between the experimental and TD-DFT absorption spectra of IO, OIO and HOI. Note that although the TD-DFT method is not designed to predict ro-vibrational structure, the spectral positions of the electronic bands and the average absorption cross sections are in reasonable agreement with the experiment, even in the case of open shell species like IO and OIO. Higher iodine oxides are closed shell molecules and the accuracy of the transitions is expected to be similar to the result for HOI.

2.3. Photolysis rate calculations

In this study we employ the global 3D model CAM-Chem (Community Atmospheric Model with chemistry, version 4.0), included in the CESM framework (Community Earth System Model) (Lamarque et al., 2012), to estimate the photolysis rate (J) of the different I_xO_y species according to their computed absorption cross-section, constrained by the experimental data at 532 and 355 nm. CAM-Chem has been configured with a 2.5º longitude by 1.9º latitude spatial resolution and 26 vertical level (from the surface to up to 40 km). The model was run in the specified dynamics mode (Lamarque et al., 2012), using offline meteorological fields from a previous free-running climatic simulation (Fernandez et al., 2014; Saiz-Lopez et al., 2015). CAM-Chem implements a state-of-the-art halogen chemistry scheme (Fernandez et al., 2014; Saiz-Lopez et al., 2014; Saiz-Lopez et al., 2015). This chemical scheme is fed by both organic and inorganic halogen emission sources (Ordóñez et al., 2012; MacDonald et al., 2014). Saiz-Lopez and co-workers ((Saiz-Lopez et al., 2014), hereafter SL2014) conducted two sets of simulations without and with the photolysis of I_xO_y oxides in CAM-Chem to evaluate the range of inorganic iodine loading, partitioning and impact in the troposphere. The photolysis of I_xO_y was based on the best available knowledge at that time on the major I_xO_y species (I_2O_2, I_2O_3 and I_2O_4) and their absorption cross sections (Gómez Martín et al., 2005; Gómez Martín et al., 2013). In this study we run photolysis simulations and compare the J values with the new cross sections to those in SL2014.

3. Results

3.1. Photolysis at 355 nm

As described in the experimental section, kinetic profiles of the growth and removal of the target iodine oxide species shown in Figure 3 were carried out in order to define the time periods with the most suitable kinetic profiles for photolysis

Field Code Changed

Deleted: 7

Field Code Changed

Field Code Changed

Field Code Changed

Field Code Changed

Field Code Changed

Field Code Changed

Field Code Changed

Field Code Changed

Field Code Changed

Field Code Changed

Field Code Changed

Field Code Changed

Field Code Changed

measurements (Figure 5). Fragmentation of iodine oxides was a significant problem in these experiments, as predicted from ionization energy calculations of larger iodine oxides to possible photofragments at 10.5 eV(Gómez Martín et al., 2020). High amounts of active iodine (IO_x = I, IO) released from reaction R12 lead to fast formation of I_xO_y and particles. Under these conditions, at long times after the peak IO and OIO (~3-5 ms), the observed signal of IO, OIO and I_xO_y is contaminated by photofragmentation of higher order iodine oxides. For this reason, great care needed to be taken to establish a time window for each species wherein higher oxides are not present, to ensure that any depletion in the mass spectrometric signal for each species is exclusively due to the removal of the species via photolysis (Figure B1). Evidence of fragmentation comes in the form of a secondary growth in the signal seen for IO and OIO (Figure 5). The delay between the excimer and the Nd:YAG photolysis laser was therefore carefully selected to coincide with a period of relatively constant signal of the desired analyte, typically a maximum for short lived species, or a slow rise for larger reaction products of interest.

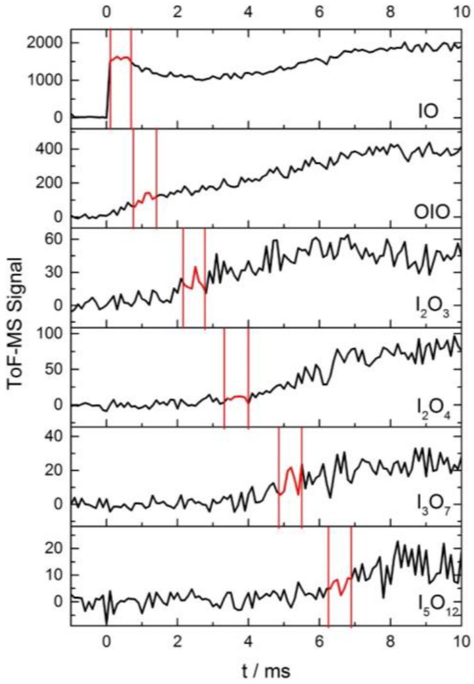

Figure 5. Time traces of IO, OIO, I_2O_3, I_2O_4, I_3O_7 and I_5O_{12} from -1-10 ms, at 1 ms intervals for a mixture of He (10 torr), O_3 and I_2 ([O_3] = 4 × 10^{14} molecule cm^{-2} [I_2] = 2.8 × 10^{14} molecule cm^{-2}) flash photolyzed by an excimer pulse at t = 0 (130 mJ pulse^{-1}). The red sections highlighted for each species correspond to the optimal delay windows for photolysis of the corresponding species for this set of conditions.

Moved (insertion) [2]

Field Code Changed

Deleted: where the

Deleted: is high, leading

In the case of IO and OIO, the photolysis delay was selected based on the location of the maxima of their kinetic profiles. Typically, this was around 1 and 2 ms for IO and OIO respectively. IO showed a clear depletion of ~20% at 355 nm (Figure 6a) corresponding to a cross section of $\sigma_{355\ \mathrm{nm,\ IO}} = (1.2 \pm 0.1) \times 10^{-18}$ cm^2 molecule^{-1} (based on an average of 3 measurements) in excellent agreement with the most recent determinations based on absorption spectroscopy (Bloss et al., 2001; Spietz et al., 2005), where the presence of an underlying absorption corresponding to a product of reactions R2, R4, R5 or R6 was accounted for (Atkinson et al., 2007) (Figure 6b). We consider the mutual consistency between our measurement and the most reliable determinations of the IO cross section at 355 nm as a validation of our method for determining the absorption cross sections of I_xO_y species.

Field Code Changed

Field Code Changed

Field Code Changed

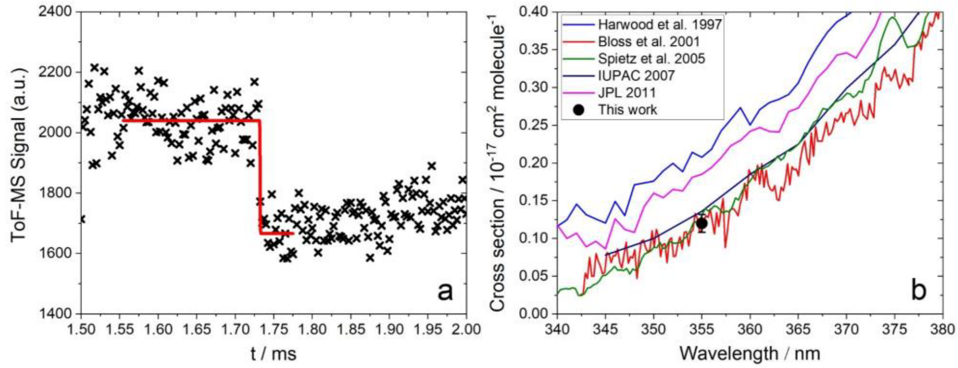

Figure 6: Panel a: measured photodepletion of IO (m/z = 143). Panel b: comparison of published absorption cross section with the absorption cross section at 355 nm determined in this work

Deleted: 6

As expected, no significant depletion was observed for OIO, with an upper limit of $\sigma_{355\ \mathrm{nm,\ OIO}} < 10^{-19}$ cm^2 molecule^{-1} based on the noise of the mass spectrometric signal at *m/z* 159. No significant depletion was observed for I_2O_3 (*m/z* =302) at 355 nm (Figure 7, top left), and an upper limit for the absorption cross section of $\sigma_{355\ \mathrm{nm,\ I2O3}} < 5 \times 10^{-20}$ cm^2 molecule^{-1} was determined based on the average noise of the I_2O_3 signal. By contrast, I_2O_4 was depleted by 355 nm photolysis by ~40% (Figure 7, top right), corresponding to a photolysis cross-section of $\sigma_{355\ \mathrm{nm,\ I2O4}} = (2.7 \pm 0.3) \times 10^{-18}$ cm^2 molecule^{-1} (based on an average of 2 measurements).

The molecular clusters I_3O_7 (*m/z* = 493) and I_5O_{12} (827) are two of the major peaks of successive mass peak progressions observed in the mass spectra in Figure 3. Experimental runs with wider spectral windows show peaks that correspond to even larger molecular clusters: I_7O_{17} (1161), I_9O_{22} (1495), $I_{11}O_{27}$ (1829) and $I_{13}O_{32}$ (2163). Notably, no mass peaks with even number of iodine atoms appear, even for higher pressures and using N_2 as carrier gas (Gómez Martín et al., 2020). It is also interesting that these peaks are separated by 334 atomic mass units, which is the value of *m/z* for I_2O_5. Although I_2O_5 is not observed in the gas phase, it is noted that as the clusters grow larger, the ratio O:I ratio tends to 2.5, reaching 2.46 for $I_{13}O_{32}$, i.e. within the range of variability of the O:I ratio of iodine oxide particles (IOPs) determined by EDX (O/I = 2.42 ± 0.05) (Saunders et al.,

Field Code Changed

Field Code Changed

2010). The prominent peak at *m/z* = 493 is the largest mass observed in our previous work on I_xO_y (Gómez Martín et al., 2013) and appears in all the spectra acquired in the course of the present work. From the observed photodepletion of I_3O_7 at 335 nm we have determined an absorption cross section of $\sigma_{355\,\mathrm{nm},\,\mathrm{I3O7}} = (5.3 \pm 1.4) \times 10^{-18}$ cm^2 molecule^{-1} (based on an average of 3 measurements) (Figure 7). The measured cross section for the I_5O_{12} cluster is $\sigma_{355\,\mathrm{nm},\,\mathrm{I5O12}} = (9.8 \pm 1) \times 10^{-18}$ cm^2 molecule^{-1} (based on an average of 2 measurements). The determined cross sections and upper limits at 355 nm are listed in Table 1.

Field Code Changed

Deleted: Table *2*Table *2*

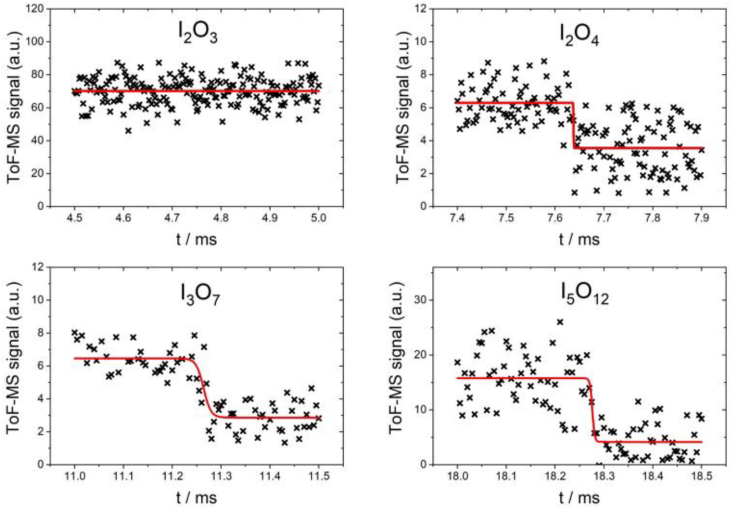

Figure 7*:* Measured photodepletion at 355 nm of I_2O_3, I_2O_4, I_3O_7 and I_5O_{12}. The laser was triggered at 4.75 ms in the I_2O_3 experiment. The red line indicates the fit to equation 2.

Fragmentation precludes determination of photolysis products at 355 nm (channels of photochemical reactions R9-R11) due to the fact that the signal arising from parent ions (which may be 355 nm photolysis products), is indistinguishable from daughter ions resulting from fragmentation of higher oxides due to the 118 nm photoionization. For any given species, possible increases in signals corresponding to products of photolysis at 355 nm are offset by the decrease in the parent ion concentration and therefore the daughter ion signal. As an example, consider I_3O_7 photolysis at 355 nm. The peaks of the possible photolysis products I_2O_3, I_2O_4, OIO and IO (referred to here as photofragments), prior to photolysis will have contributions from the parent ion signals of these species, as well as daughter ion signals of I_3O_y. Upon photolysis of I_3O_7, the concentration of I_3O_7 will decrease, causing a decrease in the parent ion signal, and therefore the daughter ion signals, resulting in turn in a net negative impact on the amplitude of all daughter ion signals. In addition to the decrease in daughter ion signals resulting from possible photofragment species, the parent ion signal for the photolabile species (IO, I_2O_4 in this example) will decrease due to direct photolysis of these species. Concurrently with the decrease in the I_3O_7 parent ion signal, there will be a positive contribution to some or all of the concentrations of possible photofragment parent ion signals. It is impossible to separate these contributions to the net change in signal magnitude, and therefore the products of these photolysis processes cannot be determined.

As indicated by reactions R10b and R11b, IO_3 (*m/z* = 175) is a potential product of I_2O_3 and I_2O_4 photolysis. However, this species has never been observed in the gas phase. According to our ab initio calculations, the ionisation potential of IO_3 is 12.1 eV, which is higher than the photoionization energy employed in the present work (10.5 eV).

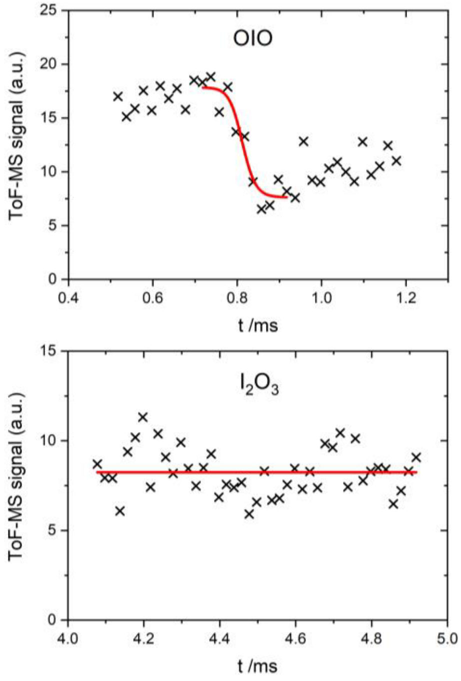

Figure 8. Measured photodepletion at 532 nm of OIO and I_2O_3. The laser was triggered at 4.5 ms in the I_2O_3 experiment.

3.2. Photolysis at 532 nm

As expected (Gómez Martín et al., 2009), OIO shows strong depletion in the 532 nm photolysis experiments (Figure 8), and it is therefore used as the actinometer at this wavelength. None of the higher order iodine oxides showed measurable depletion above the noise (as an example the I_2O_3 trace is shown in Figure 8) . Table 2 lists the upper limits to the absorption cross-sections of each species at 532 nm, determined from the signal-to-noise ratio of the recorded traces.

Field Code Changed

Table 1: Absorption cross sections of iodine oxides at 532 nm and 355 nm

Species	$\sigma_{355\ nm}$ /cm^2 molecule^{-1}	$\sigma_{532\ nm}$/cm^2 molecule^{-1}
IO	$(1.2 \pm 0.1) \times 10^{-18}$	[a]
OIO	$< 10^{-19}$	[b]
I_2O_3	$< 5 \times 10^{-19}$	$<5.0 \times 10^{-19}$
I_2O_4	$(3.9 \pm 1.2) \times 10^{-18}$	$<1.3 \times 10^{-18}$
I_3O_6	$(6.1 \pm 1.6) \times 10^{-18}$	$<1.5 \times 10^{-18}$
I_3O_7	$(5.3 \pm 1.4) \times 10^{-18}$	$<1.4 \times 10^{-18}$
I_5O_{12}	$(9.8 \pm 1.0) \times 10^{-18}$	$<1.5 \times 10^{-18}$

[a] The 0←0 band of IO is placed at 465.5 nm (Spietz et al., 2005), and therefore, there cannot be any band of ground state IO (*v*" = 0) at a longer wavelength. There is a hot band at ~530 nm (0←4), but the *v*" = 4 state is not populated at room temperature in equilibrium.

[b] Actinometer

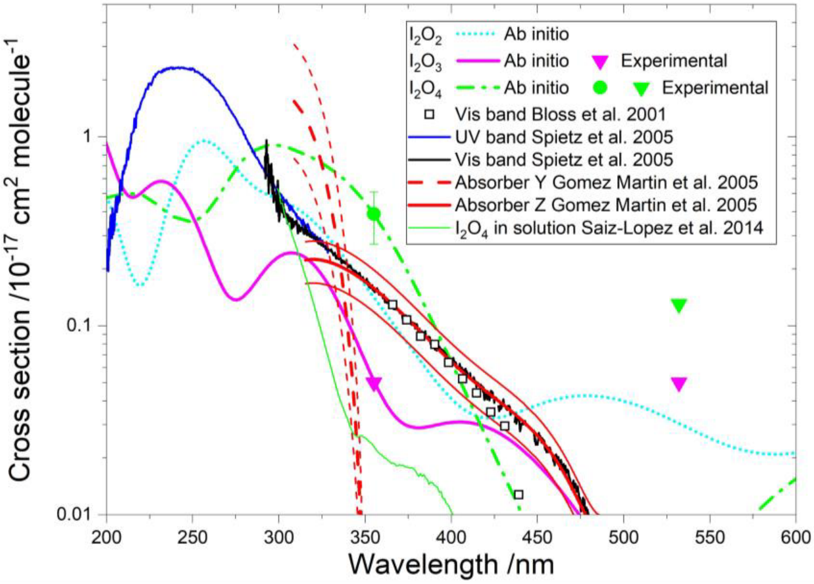

Figure 9: Absorption cross sections of I_2O_2, I_2O_3 and I_2O_4. The cyan, pink and green lines correspond to the respective ab initio spectra. The pink and green symbols indicate respectively the measured absorption cross sections of I_2O_3 and I_2O_4 (triangles indicate upper limits). The empty squares correspond to an absorption band reported by Bloss et al. (2001) in 8 nm interval averages for λ > 362 nm. The blue and black lines correspond to absorption bands reported by Spietz et al. (2005). The latter was found to be a superposition of two absorptions with different kinetic behaviour, denoted Y (dashed red line) and Z (solid red line) (Gómez Martín et al., 2005). The thin red lines represent the uncertainties of these spectra, which mainly originate from the absolute absorption cross sections of Y and Z at 322 and 356 nm respectively. A spectrum of I_2O_4 in solution is indicated in green (Saiz-Lopez et al., 2014).

Deleted: ¶

Deleted: 2

Field Code Changed

Deleted: 8

Field Code Changed

Field Code Changed

Field Code Changed

Field Code Changed

3.3. Ab initio spectra

The calculated spectra are displayed in Figure 9 (I_2O_2, I_2O_3 and I_2O_4), Figure 10 (I_3O_6 and I_3O_7), and Figure 11 (IO_3). Oscillator strengths of the electronic transitions that are responsible for the visible and UV absorptions are provided in Appendix A. The TD-DFT spectra were wavelength-shifted by applying a constant energy shift to get agreement with the experiment at 355 nm. The shifts are quite modest, within the expected error at this level of theory (Foresman and Frisch, 2015): I_2O_3 (30 kJ mol^{-1}), I_2O_4 (-12 kJ mol^{-1}), I_3O_6 (9.2 kJ mol^{-1}), I_3O_7 (-21 kJ mol^{-1}). Applying a constant energy shift means assuming that all the excited state energies are offset by a constant amount with respect to the ground state.

Field Code Changed

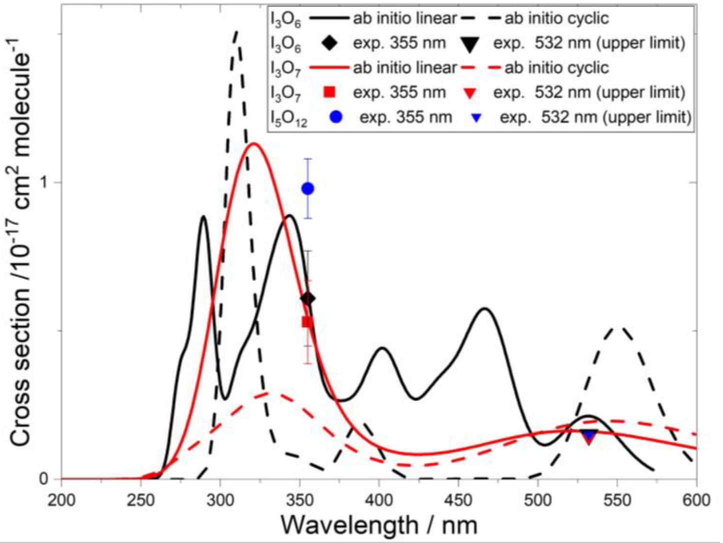

Figure 10: Absorption cross section spectra of I_3O_6 (black lines and symbols), I_3O_7 (red lines and symbols) and I_5O_{12} (blue symbols). Ab initio spectra of linear and cyclic isomers are shown by solid and dashed lines, respectively.

Deleted: 9

4. Discussion

4.1. Absorption spectra

A time-dependent broad band absorption was observed by Bloss et al. (2001) concurrently with the IO self-reaction decay, which was assigned to I_2O_2. The shape of the band was observed to be different for λ < 360 nm depending on the chemical

Field Code Changed

scheme employed to generate iodine oxides. Later, a broad band absorption with a similar spectral slope was reported (Figure 9) together with targeted UV measurements showing that the band peaks around 250 nm (Gómez Martín et al., 2005; Spietz et al., 2005). The kinetics of the absorption spectrum for λ > 310 nm were found to result from the overlap of at least two different species, one dominating the absorption below 340 nm (labelled as Y) and another one dominating from 340 nm towards the visible (labelled as Z). It was found that the kinetics of species Y was compatible with a product of the IO self-reaction, i.e. I_2O_2. By contrast Z, which would be similar to the spectrum measured by Bloss et al. for λ > 360 nm, was not compatible with a product of the IO self-reaction, and it was tentatively assigned to I_2O_3.

Gomez Martin et al. (2005) derived the cross section of the species Y and Z at 322 nm and 356 nm respectively, using an iodine mass conservation approach where the depletion of the I_2 precursor was balanced by the sum of atomic iodine contained in the oxides formed after the photolysis pulse. The cross sections were determined in a per iodine atom basis. Assuming absorbers with two iodine atoms, the spectra of Y and Z were scaled as shown in Figure 9 (Saiz-Lopez et al., 2014). Since the spectra are featureless, they can be assumed to result from bound to free transitions, justifying a unit photolysis quantum yield of the molecules generating them.

The absorption cross sections determined in this work from photodepletion of I_2O_3 and I_2O_4 at 355 nm do not confirm the previous tentative assignment of absorber Z to I_2O_3. The cross section of I_2O_4 obtained from our photodepletion experiments is in better agreement with the absorber Z. Also, it appears that the spectrum of I_2O_4 in solution largely underestimates the gas-phase spectrum. The absorption of Z at 355 nm in Figure 9 lies slightly below the I_2O_4 cross section determined in the present work, which is consistent with a contribution to Z of other I_xO_y species with x > 2 (i.e. the scaling of the spectrum should be effectively higher than the factor of 2 used by Gomez Martin et al. (2005)). In fact, the theoretical spectra of I_2O_4, I_3O_6 and I_3O_7 (Figure 9 and Figure 10) show similar shapes between 300 and 500 nm. It is very likely that the absorption band extending from 200 nm to nearly 500 nm (blue and black lines in Figure 9) results from the overlap of absorptions corresponding to several I_xO_y species. Therefore, these experimental absorption spectra are not useful for photolysis rates calculations unless further deconvolution enables separation of the different contributions.

The calculated spectra shown in Figure 9 and Figure 10 agree generally well with the experimentally determined values at 355 nm and 532 nm after small wavelength shifts indicated above. As shown in Figure 10, the upper limits from experiment are within 20% of the theoretical calculations for linear I_3O_6 and I_3O_7. Note that theoretical absorption cross section spectra for both the linear and cyclic forms (Figure 5) of I_3O_6 and I_3O_7 are shown in Figure 10. The linear forms of both species fit significantly better to the experimental values, suggesting the linear form is the one which is formed preferentially in these reactions.

4.2. Photolysis products

The likely photodissociation pathways of I_2O_3 and I_2O_4 can be elucidated by seeing how the geometry of each excited state relaxes after vertical excitation from the ground-state geometry using the TD-DFT method (see Section 2.2). In the case of

Deleted: Figure 8

Field Code Changed

Field Code Changed

Field Code Changed

Deleted: flash

Deleted: Figure 8

Field Code Changed

Deleted: Figure 8

Field Code Changed

Deleted: Figure 8

Deleted: Figure 9

Deleted: Figure 8

Deleted: Figure 8

Deleted: Figure 9

Deleted: , with only the upper limits for I_3O_6 and I_3O_7 appearing to be below the calculated values at 532 nm.

Deleted: Figure 9

I_2O_3, excitation in both the bands at 334 and 453 nm (Figure 9) produces a pronounced extension of the I–IO_3 bond, indicating photolysis leading to I + IO_3 (R10b). For I_2O_4, excitation at 667 nm and in its strong band at 324 nm produces IO + IO_3, whereas absorption in the weak band at 366 nm produces OIO + OIO.

Deleted: Figure 8

The theoretical absorption spectrum of IO_3 is shown in Figure 11, calculated at the same level of theory as described in Section 2.2. IO_3 absorbs in the tropospheric solar actinic range in two near-IR bands centered at 710 and 950 nm. There are two possible photolysis pathways:

Deleted: Figure 10

$$IO_3 + h\nu \rightarrow OIO + O \qquad \text{(R15)}$$

$$\rightarrow IO + O_2 \qquad \text{(R16)}$$

The first channel requires 180 kJ mol^{-1} to break the O_2I–O bond (not including spin-orbit coupling), corresponding to a photolytic threshold of 665 nm. R16 is closely analogous to the photolysis of OIO in its band between 500 and 600 nm, where the I atom is squeezed out from between the two O atoms in a process that overall is actually exothermic because of the strength of the newly-formed O_2 bond (Gómez Martín et al., 2009). In the same way, R16 is exothermic by 78 kJ mol^{-1}. However, there is a barrier of 145 kJ mol^{-1} involved in squeezing the IO out from between the 2 oxygen atoms. This corresponds to a photolytic threshold of 827 nm. Both of these thresholds are indicated on Figure 11. This shows that absorption across the entire 710 nm band is sufficient for photolysis via R16 to occur. If that were the case, then $J(IO_3 \rightarrow IO + O_2)$ could be as large as 0.15 s^{-1}.

Field Code Changed

Deleted: Figure 10

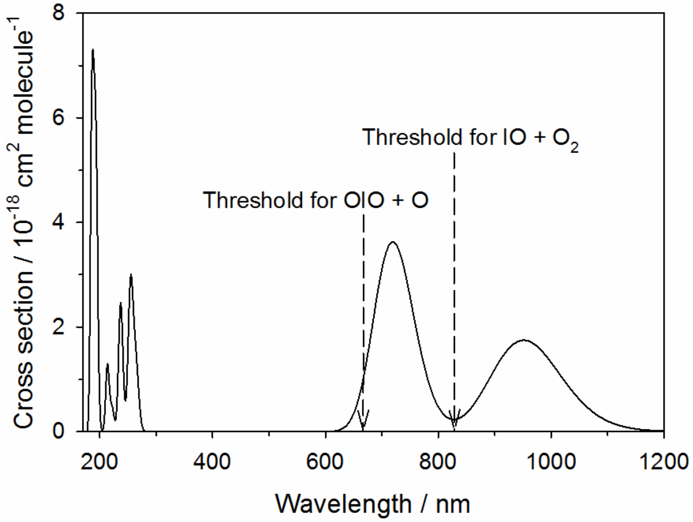

Figure 11: Absorption spectrum of IO_3 calculated at the TD/B3LYP/gen level of theory (see text for further details). The arrows indicate the energy thresholds for the two photodissociation pathways.

Deleted: 10

Photolysis via R15 is just possible in the short wavelength tail of the 710 nm band, so $J(IO_3 \rightarrow OIO + O)$ could be as large as 0.007 s^{-1}. It therefore seems likely that photolysis of IO_3 is fast and mainly produces IO.

If, however, photolysis of IO_3 is significantly slower than this upper limit, the molecule could persist in the atmosphere long enough to undergo reaction with other molecules. An intriguing possibility is that IO_3 may be a source of HIO_3. The reaction

$$IO_3 + H_2O \rightarrow HIO_3 + OH \qquad \text{(R16)}$$

is endothermic by 25 kJ mol^{-1} (14 kJ mol^{-1} according to previous work at higher level of theory (Khanniche et al., 2017b)), and so most likely does not occur. However, the reaction

Field Code Changed

$$IO_3 + HO_2 \rightarrow HIO_3 + O_2 \qquad \text{(R17)}$$

is very exothermic with a deep submerged barrier (Figure 12). A Rice-Ramsperger-Kassel-Markus (RRKM) calculation using the MESMER program (Glowacki et al., 2012) with the molecular parameters in Table 1 indicates that the rate constant of R17 is k(290 K) ~ 3 × 10^{-11} cm^3 $molecule^{-1}$ s^{-1}. Given that $[HO_2]$ is typically 3 × 10^8 molecule cm^{-3} at midday (Stone et al., 2012), IO_3 could be converted to HIO_3 with a reaction rate of ~ 0.01 s^{-1} i.e. about 15 times slower than the upper limit to the photolysis rate discussed above. R17 could therefore provide a route to HIO_3 formation, and this should be the subject of future investigation.

Deleted: Figure 11

Field Code Changed

Field Code Changed

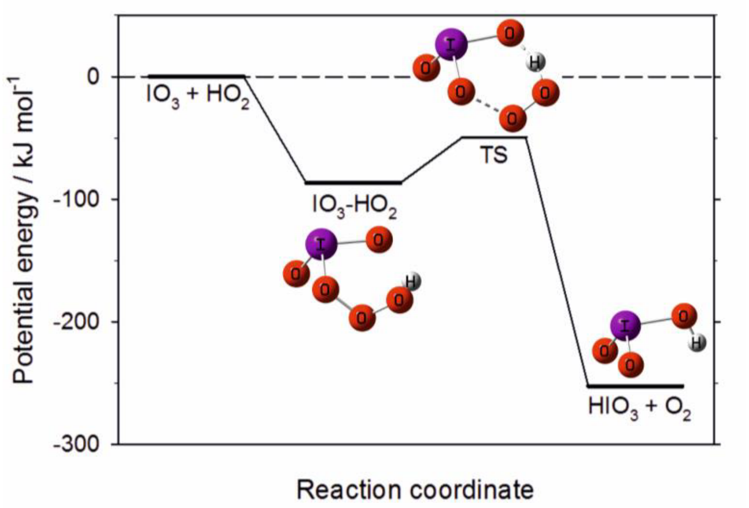

Figure 12: Potential energy surface for the reaction between IO_3 and HO_2 to produce HIO_3, calculated at the B3LYP/gen level of theory (see text for further details).

Deleted: 11

4.3. Atmospheric implications

The theoretical spectra constrained with the measurements at 355 nm and 532 nm have been implemented in CAM-Chem in order to calculate photolysis rates for I_2O_y (y = 2, 3, 4) and I_3O_7. Having anchored the theoretical absorption spectra at 355 nm, we then assume that photolysis is possible up to the dissociation limit (which is the case for all the transitions of the I_xO_y (x > 1) molecules). A conservative estimate is a factor of 2 uncertainty in the *J* values for these molecules. The main changes with respect to SL2014 are:

1. The new I_2O_2 cross sections are lower in the UV than those of the absorber Y used in SL2014 (Figure 9) and extend over a wider range of the actinic range.
2. I_2O_3 and I_2O_4 have respectively lower and higher absorption cross sections than in SL2014, as a result of replacing the absorption Z and the I_2O_4 spectrum in solution in favour of theoretical spectra constrained with experimental values. The cross section of I_2O_3 is lower, but only by a factor of ~2 in the important region between 350 nm and 450 nm. The cross sections of I_2O_4 increase by 1 order of magnitude with respect to the spectrum in solution.
3. Higher iodine oxides like I_3O_7 and I_5O_{12} not included in SL2014 also photolyze. They show bands in the green part of the spectrum (Figure 10) and therefore have higher photolysis rates than I_2O_4.

Annual zonal-average photolysis rate plots are shown in Figure 13 and Figure 14. Surface atmospheric photolysis of all the I_xO_y species is generally fastest between 30° and -30° latitude, displaying slight minima at 5° and -5° latitude due to attenuation of actinic flux by cloud cover at the intertropical convergence zone. Average I_xO_y global *J* values in the upper troposphere exhibit a maximum around 5° latitude, where solar flux is highest. At 5° latitude, I_2O_2 and I_2O_4 *J* values are largest at an altitude of 8 km. Similarly, the *J* values for I_2O_3 and I_3O_7 at 5° latitude are highest at 8 km, and then remain relatively constant above 20 km. In contrast with *J* values for I_xO_y at 5° latitude, values at mid-latitudes increase with altitude, showing no maxima at 8 km. The observed increase in *J* values at 8 km is explained by the albedo effect of cloud cover in certain regions, particularly the intertropical convergence zone, contributing to the total (incident + reflected) solar flux in these regions. Figure 13(d-f) show the percentage difference between the SL2014 *J* values and those calculated in this study. As a result of the new I_2O_2 cross sections extending across the actinic window, this species shows an increase in *J* values at all latitudes, with the largest increases seen at the poles (~300% increase), and lower increases of around 100% near the equator. I_2O_3 shows a uniform decrease of around 46% across all latitudes and altitudes, as expected from the approximately uniform decrease of the new spectrum with respect to absorber Z, which was taken as I_2O_3 in SL2014. I_2O_4 exhibits the largest increase in *J* values across all latitudes, ranging from 750% at 40 km between -30° and 30° latitude, up to increases above 1000% at the poles. Photolytic lifetimes of I_xO_y species in the troposphere vary from a few seconds for the most photolabile species, i.e. I_3O_7, to several minutes for I_2O_3, which has the smallest absorption cross-sections in the actinic region and the smallest *J* values of the species in this study. Mid and high-latitudes exhibit particularly low *J* surface values and encompass many coastal regions where active iodine concentrations are high and iodine-driven particle formation has been reported (Saiz-Lopez et al., 2012b).

Deleted: Figure 8

Deleted: Figure 9

Deleted: Figure 12

Deleted: Figure 13

Deleted: Figure 12

Field Code Changed

Photolysis of higher iodine oxides (R9-R11) competes with gas-to-particle formation (R7) and recycles IO_x, which participates in ozone depleting cycles (e.g. R1-R3). Therefore, higher *J* values at the surface tend to hinder particle formation and enhance ozone depletion. The new spectra result in decreased photolysis lifetimes of I_2O_2 (factor of ~3) and I_2O_4 (factor of ~10) and indicate that photolysis of nascent iodine clusters such as I_3O_7 and I_5O_{12} may further slow down particle formation. On the other hand, the lifetime I_2O_3 is approximately doubled, which increases the chances of participating in other reactions, including clustering with other I_xO_y. Whether this may balance the decrease in the photolysis lifetimes of other species or not

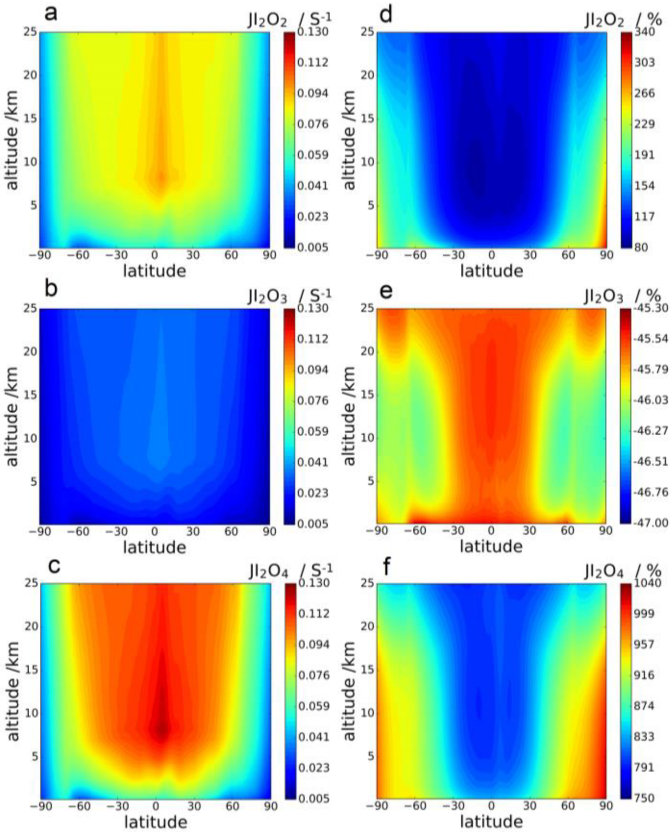

Figure 13: Annual zonal average J value vertical profiles for I_2O_2, I_2O_3 and I_2O_4 (panels a, b and c, respectively; note that the colour scale is the same for these three panels) and the percentage change between the SL2014 annual zonal average J value vertical profiles, and the profiles in this study (panels d, e and f, respectively)

Deleted: 12

remains to be studied in future work. I_2O_3 is believed to be an important iodine reservoir and key intermediate in the formation of new particles (Gómez Martín et al., 2013; Saiz-Lopez et al., 2014), but there is a substantial lack of mechanistic information about iodine oxides and how they may convert (or not) into HIO_3.

Field Code Changed

Field Code Changed

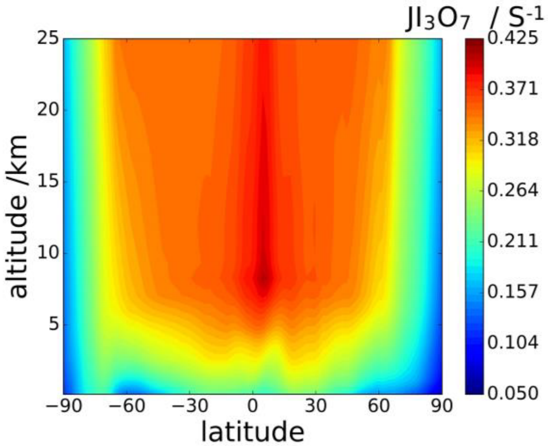

Figure 14: Annual zonal average vertical J value profile for I_3O_7 (not included in SL2014)

Deleted: 13

Another active iodine chemistry region is the tropical upper troposphere - lower stratosphere region (UTLS), where significant concentrations of iodine exist (Koenig et al., 2020) as a result of strong convection carrying iodine precursors emitted at the ocean surface (mainly CH_3I). The effect of the new spectra on the *J* values in this region is similar to the effect at the surface, although the changes are less pronounced. In the UTLS, I_xO_y molecules play the role of iodine reservoirs and, as a result of the enhanced actinic flux (see *J* maxima between 8 and 17 km around the equator in Figures 12 and 13), their photolysis has a significant impact on ozone depletion in this climatically sensitive region (Saiz-Lopez et al., 2012a). Iodine recycling in aerosol is believed to play an important role in explaining observed concentrations of gas-phase IO_x (Koenig et al., 2020). The form in which gas-phase iodine (oxides, oxyacids or nitrate) is taken up in sulphate aerosol may also determine the extent to which iodine can return to the gas phase.

Deleted: hotspot of iodine chemistry

Field Code Changed

Field Code Changed

Field Code Changed

To investigate with more detail the effect of the new spectra on particle formation, iodine speciation in aerosol and ozone depletion, the iodine chemistry scheme in CAM-Chem needs to be expanded to include the photolysis products and yields of I_xO_y photolysis reactions, as well as the reactions of the possible photoproducts, which are poorly known. New laboratory and theoretical work is required to solve these uncertainties. The mechanism of IOP formation remains controversial, with two possible pathways proposed via I_xO_y and HIO_3. Work on the IOP formation mechanism conducted in the course of this research will be published elsewhere. Future laboratory measurements of I_xO_y spectra and kinetics may benefit from a multiplexed approach where tuneable photoionization mass spectrometry, absorption spectroscopy and multi-wavelength laser photodepletion are used concurrently. A follow up modelling study will be conducted with an updated mechanism for atmospheric iodine chemistry, including the photochemistry outlined in this paper, as well as a chemical scheme for IOP formation.

5. Conclusion

The photodepletion laboratory experiments reported in this work confirm that I_xO_y species are photolabile, and therefore supports the $J(I_xO_y)$ scenario in ASL2014, with important consequences for ozone depletion. The values of the absorption cross sections obtained at 355 nm and 532 nm have been employed to revisit the assignment of absorption bands in previous work. Also, comparison between theoretical spectra and measurements gives some clues about the geometry of the molecules. I_2O_3 has a smaller absorption cross-section in the actinic region than previously thought, which may facilitate other reactions, including clustering to form new particles. Other I_xO_y species have larger absorption cross-sections in the actinic region, resulting in rapid photolysis to smaller iodine-containing molecules. Possible photolysis products include IO_3, which could be a precursor of HIO_3 in the marine boundary layer. These new findings highlight the need for new experimental and theoretical studies, particularly investigating the products of these photochemical processes, as well as the effect on IOPs (and therefore cloud condensation nuclei) formation.

Author contribution. A. S.-L. devised the research. J. C. G. M., M. A. B. and J. M. C. P. designed the experimental set up, and T. R. L. carried out the experiments and analysed the data; J. M. C. P. and J. C. G. M. carried out electronic structure and master equation calculations; C. A. C. carried out radiative transfer calculations; T. R. L. and J. C. G. M. wrote the manuscript with contributions from all co-authors.

Code/Data availability. The data that support the findings of this study are available from the corresponding authors on reasonable request.

Competing interests. The authors declare that they have no conflict of interest.

Acknowledgements. This study has received funding from the European Research Council Executive Agency under the European Union's Horizon 2020 Research and Innovation program (Project 'ERC-2016-COG 726349 CLIMAHAL'). J. C. G. M. acknowledges financial support from the State Agency for Research of the Spanish MCIU through the "Center of Excellence Severo Ochoa" award to the Instituto de Astrofísica de Andalucía (SEV-2017-0709) and the Ramon y Cajal program (RYC-2016-19570). J. C. G. M. and A. S.-L. acknowledge support of the publication fee by the CSIC Open Access Publication Support Initiative through its Unit of Information Resources for Research (URICI).

References

Ashworth, S. H., Allan, B. J., and Plane, J. M. C.: High resolution spectroscopy of the OIO radical: Implications for the ozone-depleting potential of iodine, Geophys. Res. Lett., 29, 95-91-95-94, doi: 10.1029/2001gl013851, 2002.

Atkinson, R., Baulch, D. L., Cox, R. A., Crowley, J. N., Hampson, R. F., Hynes, R. G., Jenkin, M. E., Rossi, M. J., and Troe, J.: Evaluated kinetic and photochemical data for atmospheric chemistry: Volume III – gas phase reactions of inorganic halogens, Atmos. Chem. Phys., 7, 981-1191, doi: 10.5194/acp-7-981-2007, 2007.

Baeza-Romero, M. T., Blitz, M. A., Goddard, A., and Seakins, P. W.: Time-of-flight mass spectrometry for time-resolved measurements: Some developments and applications, Int. J. Chem. Kinet., 44, 532-545, doi: 10.1002/kin.20620, 2012.

Bloss, W. J., Rowley, D. M., Cox, R. A., and Jones, R. L.: Kinetics and Products of the IO Self-Reaction, J. Phys. Chem. A, 105, 7840-7854, doi: 10.1021/jp0044936, 2001.

Burkholder, J. B., Sander, S. P., Abbat, J., Barker, J. R., Huie, R. E., Kolb, C. E., Kurylo, M. J., Orkin, V. L., Wilmouth, D. M., and Wine, P. H.: Chemical Kinetics and Photochemical Data for Use in Atmospheric Studies, Evaluation No. 18 JPL-NASA, Pasadena, 2015.

Burrows, J., Richter, A., Dehn, A., Deters, B., Himmelmann, S., Voigt, S., and Orphal, J.: Atmospheric remote-sensing reference data from GOME—2. Temperature-dependent absorption cross sections of O3 in the 231–794 nm range, J. Quant. Spectrosc. Radiat. Transfer, 61, 509-517, doi: 10.1016/S0022-4073(98)00037-5, 1999.

Canneaux, S., Xerri, B., Louis, F., and Cantrel, L.: Theoretical Study of the Gas-Phase Reactions of Iodine Atoms (2P3/2) with H2, H2O, HI, and OH, J. Phys. Chem. A, 114, 9270-9288, doi: 10.1021/jp104163t, 2010.

Carpenter, L. J., MacDonald, S. M., Shaw, M. D., Kumar, R., Saunders, R. W., Parthipan, R., Wilson, J., and Plane, J. M. C.: Atmospheric iodine levels influenced by sea surface emissions of inorganic iodine, Nat. Geosci., 6, 108-111, doi: 10.1038/ngeo1687, 2013.

Chance, R., Baker, A. R., Carpenter, L., and Jickells, T. D.: The distribution of iodide at the sea surface, Environ. Sci. Process Impacts, 16, 1841-1859, doi: 10.1039/c4em00139g, 2014.

Cox, R. A., and Coker, G. B.: Absorption Cross section and Kinetics of IO in the Photolysis of CH_3I in the presence of Ozone, J. Phys. Chem., 87, 4478-4484., doi: 10.1021/j100245a030, 1983.

Cuevas, C. A., Maffezzoli, N., Corella, J. P., Spolaor, A., Vallelonga, P., Kjær, H. A., Simonsen, M., Winstrup, M., Vinther, B., Horvat, C., Fernandez, R. P., Kinnison, D., Lamarque, J.-F., Barbante, C., and Saiz-Lopez, A.: Rapid increase in atmospheric iodine levels in the North Atlantic since the mid-20th century, Nat. Commun., 9, 1452, doi: 10.1038/s41467-018-03756-1, 2018.

Dennington, R., Keith, T. A., and Millam, J. M.: GaussView, Version 6.1, Semichem Inc., Shawnee Mission, KS, 2016.

Fernandez, R. P., Salawitch, R., Kinnison, D., Lamarque, J.-F., and Saiz-lopez, A.: Bromine partitioning in the tropical tropopause layer: implications for stratospheric injection, Atmos. Chem. Phys., doi: 10.5194/acp-14-13391-2014, 2014.

Foresman, J. B., and Frisch, Æ.: Exploring Chemistry with Electronic Structure Methods 3rd. Ed. , Gaussian, Inc., Wallingford, CT, USA, 2015.

Frisch, M. J., Trucks, G. W., Schlegel, H. B., Scuseria, G. E., Robb, M. A., Cheeseman, J. R., Scalmani, G., Barone, V., Petersson, G. A., Nakatsuji, H., Li, X., Caricato, M., Marenich, A. V., Bloino, J., Janesko, B. G., Gomperts, R., Mennucci, B., Hratchian, H. P., Ortiz, J. V., Izmaylov, A. F., Sonnenberg, J. L., Williams-Young, D., Ding, F., Lipparini, F., Egidi, F., Goings, J., Peng, B., Petrone, A., Henderson, T., Ranasinghe, D., Zakrzewski, V. G., J. Gao, N. R., Zheng, G., Liang, W., Hada, M., Ehara, M., Toyota, K., Fukuda, R., Hasegawa, J., Ishida, M., Nakajima, T., Honda, Y., Kitao, O., Nakai, H., Vreven, T., Throssell, K., J. A. Montgomery, J., Peralta, J. E., Ogliaro, F., Bearpark, M. J., Heyd, J. J., Brothers, E. N., Kudin, K. N., Staroverov, V. N., Keith, T. A., Kobayashi, R., Normand, J., Raghavachari, K., Rendell, A. P., Burant, J. C., Iyengar, S. S., Tomasi, J., Cossi, M., Millam, J. M., Klene, M., Adamo, C., Cammi, R., Ochterski, J.

W., Martin, R. L., Morokuma, K., Farkas, O., Foresman, J. B., and Fox, D. J.: Gaussian 16, Revision B.01, Gaussian, Inc., Wallingford, CT, USA, 2016.

Galvez, O., Gómez Martín, J. C., Gomez, P. C., Saiz-Lopez, A., and Pacios, L. F.: A theoretical study on the formation of iodine oxide aggregates and monohydrates, Phys. Chem. Chem. Phys., 15, 15572-15583, doi: 10.1039/c3cp51219c, 2013.

Glowacki, D. R., Liang, C.-H., Morley, C., Pilling, M. J., and Robertson, S. H.: MESMER: An Open-Source Master Equation Solver for Multi-Energy Well Reactions, J. Phys. Chem. A, 116, 9545-9560, doi: 10.1021/jp3051033, 2012.

Glukhovtsev, M. N., Pross, A., McGrath, M. P., and Radom, L.: Extension of Gaussian-2 (G2) theory to bromine- and iodine-containing molecules: Use of effective core potentials, J. Chem. Phys., 103, 1878-1885, doi: 10.1063/1.469712, 1995.

Gómez Martín, J. C., Spietz, P., and Burrows, J. P.: Spectroscopic studies of the I_2/O_3 photochemistry: Part 1: Determination of the absolute absorption cross sections of iodine oxides of atmospheric relevance, J. Photochem. Photobiol., A, 176, 15-38, doi: 10.1016/j.jphotochem.2005.09.024, 2005.

Gómez Martín, J. C., Spietz, P., and Burrows, J. P.: Kinetic and Mechanistic Studies of the I_2/O_3 Photochemistry, J. Phys. Chem. A, 111, 306-320, doi: 10.1021/jp061186c, 2007.

Gómez Martín, J. C., Ashworth, S. H., Mahajan, A. S., and Plane, J. M. C.: Photochemistry of OIO: Laboratory study and atmospheric implications, Geophys. Res. Lett., 36, L09802, doi: 10.1029/2009GL037642, 2009.

Gómez Martín, J. C., Galvez, O., Baeza-Romero, M. T., Ingham, T., Plane, J. M. C., and Blitz, M. A.: On the mechanism of iodine oxide particle formation, Phys. Chem. Chem. Phys., 15, 15612-15622, doi: 10.1039/c3cp51217g, 2013.

Gómez Martín, J. C., Garraway, S. A., and Plane, J. M. C.: Reaction Kinetics of Meteoric Sodium Reservoirs in the Upper Atmosphere, J. Phys. Chem. A, 120, 1330-1346, doi: 10.1021/acs.jpca.5b00622, 2016.

Gómez Martín, J. C., Lewis, T., Blitz, M. A., Plane, J. M., Kumar, M., Francisco, J. S., and Saiz-Lopez, A.: New insights into atmospheric iodine gas-to-particle conversion, Nat. Commun., Accepted, 2020.

Hammaecher, C., Canneaux, S., Louis, F., and Cantrel, L.: A Theoretical Study of the H-Abstraction Reactions from HOI by Moist Air Radiolytic Products (H, OH, and O (3P)) and Iodine Atoms (2P3/2), J. Phys. Chem. A, 115, 6664-6674, doi: 10.1021/jp202760u, 2011.

Harwood, M. H., Burkholder, J. B., Hunter, M., Fox, R. W., and Ravishankara, A. R.: Absorption Cross Sections and Self-Reaction Kinetics of the IO Radical, J. Phys. Chem. A, 101, 853-863, doi: 10.1021/jp962429b, 1997.

Hoffmann, T., O'Dowd, C. D., and Seinfeld, J. H.: Iodine oxide homogeneous nucleation: An explanation for coastal new particle production, Geophys. Res. Lett., 28, 1949-1952, doi: 10.1029/2000GL012399, 2001.

Jimenez, J. L., Bahreini, R., Cocker, D. R., III, Zhuang, H., Varutbangkul, V., Flagan, R. C., Seinfeld, J. H., O'Dowd, C. D., and Hoffmann, T.: New particle formation from photooxidation of diiodomethane (CH2I2), J. Geophys. Res. [Atmos.], 108, 4318, doi: 10.1029/2002JD002452, 2003.

Joseph, D. M., Ashworth, S. H., and Plane, J. M. C.: The absorption cross-section and photochemistry of OIO, Journal of Photochemistry and Photobiology A: Chemistry, 176, 68-77, doi: https://doi.org/10.1016/j.jphotochem.2005.09.003, 2005.

Kaltsoyannis, N., and Plane, J. M. C.: Quantum chemical calculations on a selection of iodine-containing species (IO, OIO, INO3, (IO)2, I2O3, I2O4 and I2O5) of importance in the atmosphere, Phys. Chem. Chem. Phys., 10, 1723-1733, doi: 10.1039/b715687c, 2008.

Khanniche, S., Louis, F., Cantrel, L., and Černušák, I.: Thermochemistry of HIO2 Species and Reactivity of Iodous Acid with OH Radical: A Computational Study, ACS Earth Space Chem., 1, 39-49, doi: 10.1021/acsearthspacechem.6b00010, 2017a.

Khanniche, S., Louis, F., Cantrel, L., and Černušák, I.: Investigation of the Reaction Mechanism and Kinetics of Iodic Acid with OH Radical Using Quantum Chemistry, ACS Earth Space Chem., 1, 227-235, doi: 10.1021/acsearthspacechem.7b00038, 2017b.

Koenig, T. K., Baidar, S., Campuzano-Jost, P., Cuevas, C. A., Dix, B., Fernandez, R. P., Guo, H., Hall, S. R., Kinnison, D., Nault, B. A., Ullmann, K., Jimenez, J. L., Saiz-Lopez, A., and Volkamer, R.: Quantitative detection of iodine in the stratosphere, Proc. Nat. Acad. Sci. U.S.A., 117, 1860-1866, doi: 10.1073/pnas.1916828117, 2020.

Kumar, M., Saiz-Lopez, A., and Francisco, J. S.: Single-Molecule Catalysis Revealed: Elucidating the Mechanistic Framework for the Formation and Growth of Atmospheric Iodine Oxide Aerosols in Gas-Phase and Aqueous Surface Environments, J. Am. Chem. Soc., 140, 14704-14716, doi: 10.1021/jacs.8b07441, 2018.

Kung, A. H., Young, J. F., and Harris, S. E.: Generation of 1182-Å radiation in phase-matched mixtures of inert gases, Appl. Phys. Lett., 22, 301-302, doi: 10.1063/1.1654647, 1973.

Lamarque, J.-F., Emmons, L., Hess, P., Kinnison, D. E., Tilmes, S., Vitt, F., Heald, C., Holland, E. A., Lauritzen, P., and Neu, J.: CAM-chem: Description and evaluation of interactive atmospheric chemistry in the Community Earth System Model, Geosci. Model Dev., 5, 369, doi: 10.5194/gmd-5-369-2012, 2012.

Laszlo, B., Kurylo, M. J., and Huie, R. E.: Absorption cross sections, kinetics of formation, and self-reaction of the IO radical produced via the laser photolysis of $N_2O/I_2/N_2$ mixtures, J. Phys. Chem., 99, 11701-11707, doi: 10.1021/j100030a013, 1995.

Lewis, T., Heard, D. E., and Blitz, M. A.: A novel multiplex absorption spectrometer for time-resolved studies, Rev. Sci. Instrum., 89, 024101, doi: 10.1063/1.5006539, 2018.

MacDonald, S. M., Gómez Martín, J. C., Chance, R., Warriner, S., Saiz-Lopez, A., Carpenter, L. J., and Plane, J. M. C.: A laboratory characterisation of inorganic iodine emissions from the sea surface: dependence on oceanic variables and parameterisation for global modelling, Atmos. Chem. Phys., 14, 5841-5852, doi: 10.5194/acp-14-5841-2014, 2014.

Mahon, R., McIlrath, T., Myerscough, V., and Koopman, D.: Third-harmonic generation in argon, krypton, and xenon: Bandwidth limitations in the vicinity of Lyman-&#945, IEEE J. Quantum Electron., 15, 444-451, doi: 10.1109/jqe.1979.1070036, 1979.

McFiggans, G., Coe, H., Burgess, R., Allan, J., Cubison, M., Alfarra, M. R., Saunders, R., Saiz-Lopez, A., Plane, J. M. C., Wevill, D. J., Carpenter, L. J., Rickard, A. R., and Monks, P. S.: Direct evidence for coastal iodine particles from Laminaria macroalgae - linkage to emissions of molecular iodine, Atmos. Chem. Phys., 4, 701-713, doi: 10.5194/acp-4-701-2004, 2004.

Ordóñez, C., Lamarque, J.-F., Tilmes, S., Kinnison, D. E., Atlas, E. L., Blake, D. R., Sousa Santos, G., Brasseur, G., and Saiz-Lopez, A.: Bromine and iodine chemistry in a global chemistry-climate model: description and evaluation of very short-lived oceanic sources, Atmos. Chem. Phys., 12, 1423-1447, doi: 10.5194/acp-12-1423-2012, 2012.

Peterson, K. A.: A theoretical study of the low-lying electronic states of OIO and the ground states of IOO and OIO−, Mol. Phys., 108, 393-408, doi: 10.1080/00268970903508548, 2010.

Pirjola, L., O'Dowd, C., Yoon, Y. J., and Sellegri, K.: Modelling Iodine Particle Formation and Growth from Seaweed in a Chamber, Environ. Chem., 2, 271-281, doi: 10.1071/EN05075, 2005.

Prados-Roman, C., Cuevas, C. A., Fernandez, R. P., Kinnison, D. E., Lamarque, J. F., and Saiz-Lopez, A.: A negative feedback between anthropogenic ozone pollution and enhanced ocean emissions of iodine, Atmos. Chem. Phys., 15, 2215-2224, doi: 10.5194/acp-15-2215-2015, 2015.

Saiz-Lopez, A., and Plane, J. M. C.: Novel iodine chemistry in the marine boundary layer, Geophys. Res. Lett., 31, L04112, doi: 10.1029/2003GL019215, 2004.

Saiz-Lopez, A., Saunders, R., Joseph, D., Ashworth, S., and Plane, J.: Absolute absorption cross-section and photolysis rate of I 2, Atmos. Chem. Phys., 4, 1443-1450, doi: 10.5194/acp-4-1443-2004, 2004.

Saiz-Lopez, A., Lamarque, J. F., Kinnison, D. E., Tilmes, S., Ordóñez, C., Orlando, J. J., Conley, A. J., Plane, J. M. C., Mahajan, A. S., Sousa Santos, G., Atlas, E. L., Blake, D. R., Sander, S. P., Schauffler, S., Thompson, A. M., and Brasseur, G.: Estimating the climate significance of halogen-driven ozone loss in the tropical marine troposphere, Atmos. Chem. Phys., 12, 3939-3949, doi: 10.5194/acp-12-3939-2012, 2012a.

Saiz-Lopez, A., Plane, J. M., Baker, A. R., Carpenter, L. J., von Glasow, R., Martin, J. C., McFiggans, G., and Saunders, R. W.: Atmospheric chemistry of iodine, Chem. Rev., 112, 1773-1804, doi: 10.1021/cr200029u, 2012b.

Saiz-Lopez, A., Fernandez, R. P., Ordóñez, C., Kinnison, D. E., Gómez Martín, J. C., Lamarque, J. F., and Tilmes, S.: Iodine chemistry in the troposphere and its effect on ozone, Atmos. Chem. Phys., 14, 13119-13143, doi: 10.5194/acp-14-13119-2014, 2014.

Saiz-Lopez, A., Baidar, S., Cuevas, C. A., Koenig, T., Fernandez, R. P., Dix, B., Kinnison, D. E., Lamarque, J.-F., Rodriguez-Lloveras, X., and Campos, T. L.: Injection of iodine to the stratosphere, Geophys. Res. Lett., 42, 6852-6859, doi: 10.1002/2015GL064796, 2015.

Sander, S. P., Abbatt, J., Barker, J. R., Burkholder, J. B., Friedl, R. R., Golden, D. M., Huie, R. E., Kolb, C. E., Kurylo, M. J., Moortga, G. K., Orkin, V. L., and Wine, P. H.: Chemical Kinetics and Photochemical Data for Use in Atmospheric Studies, Evaluation Number 17, Jet Propulsion Laboratory, Pasadena, USA, 2011.

Saunders, R. W., Mahajan, A. S., Gómez Martín, J. C., Kumar, R., and Plane, J. M. C.: Studies of the Formation and Growth of Aerosol from Molecular Iodine Precursor, Z. Phys. Chem., 224, 1095-1117, doi: 10.1524/zpch.2010.6143, 2010.

Sherwen, T., Evans, M. J., Carpenter, L. J., Andrews, S. J., Lidster, R. T., Dix, B., Koenig, T. K., Sinreich, R., Ortega, I., Volkamer, R., Saiz-Lopez, A., Prados-Roman, C., Mahajan, A. S., and Ordóñez, C.: Iodine's impact on tropospheric oxidants: a global model study in GEOS-Chem, Atmos. Chem. Phys., 16, 1161-1186, doi: 10.5194/acp-16-1161-2016, 2016.

Sipilä, M., Sarnela, N., Jokinen, T., Henschel, H., Junninen, H., Kontkanen, J., Richters, S., Kangasluoma, J., Franchin, A., Peräkylä, O., Rissanen, M. P., Ehn, M., Vehkamäki, H., Kurten, T., Berndt, T., Petäjä, T., Worsnop, D., Ceburnis, D., Kerminen, V.-M., Kulmala, M., and O'Dowd, C.: Molecular-scale evidence of aerosol particle formation via sequential addition of HIO3, Nature, 537, 532-534, doi: 10.1038/nature19314, 2016.

Spietz, P., Gómez Martín, J. C., and Burrows, J. P.: Spectroscopic studies of the I2/O3 photochemistry: Part 2. Improved spectra of iodine oxides and analysis of the IO absorption spectrum, J. Photochem. Photobiol., A, 176, 50-67, doi: 10.1016/j.jphotochem.2005.08.023, 2005.

Stone, D., Whalley, L. K., and Heard, D. E.: Tropospheric OH and HO2 radicals: field measurements and model comparisons, Chem. Soc. Rev., 41, 6348-6404, doi: 10.1039/c2cs35140d, 2012.

Stratmann, R. E., Scuseria, G. E., and Frisch, M. J.: An efficient implementation of time-dependent density-functional theory for the calculation of excitation energies of large molecules, J. Chem. Phys., 109, 8218-8224, doi: 10.1063/1.477483, 1998.

Tucceri, M. E., Hölscher, D., Rodriguez, A., Dillon, T. J., and Crowley, J. N.: Absorption cross section and photolysis of OIO, Phys. Chem. Chem. Phys., 8, 834-846, doi: 10.1039/b512702e, 2006.

Vandaele, A. C., Hermans, C., Simon, P. C., Carleer, M., Colin, R., Fally, S., Mérienne, M. F., Jenouvrier, A., and Coquart, B.: Measurements of the NO_2 absorption cross-section from 42 000 cm^{-1} to 10 000 cm^{-1} (238–1000 nm) at 220 K and 294 K, J. Quant. Spectrosc. Radiat. Transfer, 59, 171-184, doi: 10.1016/S0022-4073(97)00168-4, 1998.

Wei, N., Hu, C., Zhou, S., Ma, Q., Mikuška, P., Večeřa, Z., Gai, Y., Lin, X., Gu, X., Zhao, W., Fang, B., Zhang, W., Chen, J., Liu, F., Shan, X., and Sheng, L.: VUV photoionization aerosol mass spectrometric study on the iodine oxide particles formed from O3-initiated photooxidation of diiodomethane (CH2I2), RSC Adv., 7, 56779-56787, doi: 10.1039/c7ra11413c, 2017.

APPENDIX A1. Molecular geometries and parameters of iodine oxides at B3LYP/6-311+G(2d,p) (+AE) level of theory and benchmarking of the TD-DFT method for iodine oxides

Table A1: Molecular properties of I_2O_3, I_2O_4, I_3O_6 (cyclic), I_3O_6 (linear), I_3O_7 (cyclic), I_3O_7 (linear), IO_3 and the transition state for dissociation of IO_3 to IO + O_2 (illustrated in Figure A1); and the stationary points on the IO_3 + HO_2 surface (Figure 12).

Molecule	**Cartesian co-ordinates /Å ^{a}**	**Rotational constants /GHz ^{a}**	**Vibrational frequencies /cm^{-1} ^{a}**
I_2O_3	I, -0.009, -0.201, -0.192 O, -1.208, -0.160, 1.377 I, -0.583, 0.643, 3.128 O, 0.427, 1.521, -0.391 O, 1.423, -1.065, 0.438	4.46970, 0.57042, 0.55739	44, 88, 241, 256, 299, 450, 624, 872, 902
I_2O_4	O, -1.655, -0.203, 1.563 I, 0.046, 0.313, 1.770 O, 0.699, 0.048, -0.103 O, 0.936, -0.982, 2.619 I, -0.385, -0.913, -1.502 O, -1.272, 0.428, -2.370	3.55600, 0.49098, 0.47135	48, 67, 92, 164, 248, 260, 308, 444, 538, 812, 874, 906
I_3O_6 (cyclic)	I, 1.335, -1.791, -0.031 O, 1.569, 0.091, -0.823 O, 3.064, -2.228, 0.378 I, 1.319, 1.750 , 0.186 O, -0.279, 1.411, 0.952 O, 1.051, 2.850, -1.192 I, -2.620, -0.026, 0.066 O, -1.412, -1.310, -0.437 O, -4.280, -0.729, -0.202	0.44642, 0.26455, 0.17279	18, 26, 54,59, 66, 70, 87, 107, 116, 171, 202, 274, 295, 319, 444, 563, 783, 804, 814, 843, 898
I_3O_6 (linear)	O, -0.860, 0.445, 0.841 I, -0.142, -0.977, -0.191 O, 1.698, -0.828, 0.694 O, -2.369, -1.079, -0.706 I, 3.054, 0.513, 0.198 O, 2.321, 1.165, -1.301 O, 4.415, -0.561, -0.236 I, -3.219, 0.313, 0.228 O, -3.185, 1.803, -0.797	1.40546, 0.15363, 0.14491	21, 33, 60, 69, 85, 98, 122, 166, 184, 262, 268, 302, 313, 343, 442, 565, 664, 699, 843, 871, 903
I_3O_7 (cyclic)	I, 1.050, -1.602, -0.490 O, 1.254, 1.127, -0.500 O, 1.159, -3.334, -0.902 I, 0.374, 2.634, 0.070 O, -1.810, 0.925, 0.501	0.43718, 0.25525, 0.17036	29, 49, 61, 66, 79, 82, 90, 111, 123, 171, 186, 262, 279, 302, 308, 324, 494,

	O, 1.558, 4.011, -0.093 I, -2.237, -0.789, 0.151 O, 0.594, -1.505, 1.245 O, -3.595, -0.762, -1.001 O, -0.813, -1.235, -1.152		566, 782, 807, 852, 862, 905, 909
I_3O_7 (linear)	O, 4.334, 1.318, 0.098 I, 3.552, -0.283, 0.217 O, 1.828, 0.194, 0.994 O, 2.970, -0.766, -1.411 I, 0.004, 0.013, 0.002 O, -1.823, -0.085, -0.997 O, 0.008, -1.794, 0.247 I, -3.543, -0.351, -0.118 O, -2.958, -0.382, 1.579 O, -4.337, 1.219, -0.426	2.11361, 0.11760, 0.11718	21, 25, 33, 44, 46, 60, 84, 140, 186, 203, 263, 266, 296, 312, 320, 418, 433, 552, 635, 759, 867, 867, 901, 902
IO_3	I, 0.080, 1.235, 0.000 O, 0.645, -0.481, 0.000 O, 0.645, 2.092, 1.486 O, 0.645, 2.092, -1.486	6.18204, 6.18204, 3.57497	258, 258, 268, 766, 766, 799
TS for $IO_3 \rightarrow IO + O_2$	I, 0.205, 0.253, -0.082 O, 1.400, -1.046, 0.249 O, -1.406, -0.589, -0.790 O, -1.419, -0.181, 0.909	8.93231, 4.04781, 3.81028	-914, 142, 252, 354, 701, 867
IO_3-HO_2 complex	I, -0.649, 0.251, 0.072 O, -0.420, -1.455, 0.587 O, -0.429, 1.299, 1.501 O, 1.098, 0.455, -0.961 O, 2.104, -0.347, -0.326 O, 2.090, -1.626, -0.927 H, 1.449, -2.095, -0.357	4.44296, 1.49686, 1.34348	64, 143, 192, 226, 297, 316, 464, 530, 568, 719, 860, 903, 938, 1453, 3638
TS from IO_3-complex to $HIO_3 + O_2$	I, 0.131, 1.178, -0.047 O, 0.550, -0.594, 0.341 O, 0.383, 2.058, 1.482 O, 1.579, 1.575, -1.172 O, 2.931, 0.475, -0.440 O, 2.661, -0.726, -0.774 H, 1.671, -0.878, -0.163	4.24271, 1.59293, 1.46409	1000*i*, 74, 225, 250, 288, 323, 377, 500, 624, 711, 823, 904, 1246, 1306, 1749
HIO_3	I, 1.574, -0.480, 0.151 O, -0.137, -0.710, -0.315 O, 2.309, 0.401, -1.439 O, 1.647, 0.832, 1.363 H, 1.792, 1.203, -1.629	5.68293, 5.36595, 3.62995	62, 258, 274, 304, 584, 871, 901, 981, 3732

[a] Calculated at the B3LYP/gen level of theory (see text)

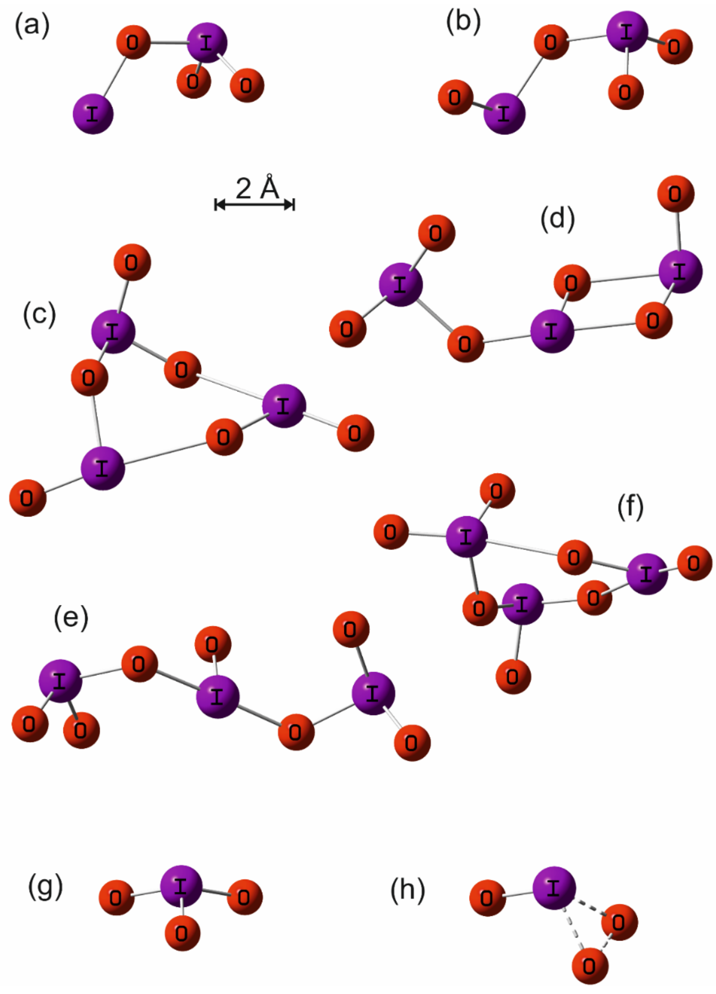

Figure A1: Molecular geometries of I_2O_3, I_2O_4, I_3O_6 (cyclic), I_3O_6 (linear), I_3O_7 (cyclic), I_3O_7 (linear), IO_3 and the transition state for dissociation of IO_3 to IO + O_2, calculated at the B3LYP/gen level of theory (see main text for details).

Table A2. Peak wavelengths and oscillators strengths (*f*) for the first 30 excited states of HOI, IO, OIO and IO_3 at the TD/B3LYP/G2 level of theory.

HOI		**IO**		**OIO**		**IO_3**	
λ / nm	*f*	λ / nm	*f*	λ / nm	*f*	λ / nm	*f*
450.3	0.0001	94003.7	0	598.9	0	1378.3	0
367.0	0.0027	513.0	0	586.8	0.0002	951.7	0.0039
224.7	0.0089	390.6	0	584.2	0.0217	951.0	0.0039
192.8	0.0478	386.7	0.0001	342.6	0.0006	719.7	0.0081
178.4	0.0999	379.4	0.0365	337.5	0	719.3	0.0081
173.3	0.072	338.5	0.0001	281.0	0	264.4	0.0027
168.9	0.1978	321.0	0.0001	278.7	0	264.4	0.0027
165.4	0.0447	244.5	0.0052	270.3	0.0027	254.9	0.0127
164.9	0.002	230.9	0.0001	262.6	0	249.4	0
161.4	0.0659	212.4	0.0006	262.0	0	246.4	0.0001
157.9	0.0003	198.7	0.0114	249.7	0.0046	246.3	0.0001
153.2	0.0056	193.5	0.0249	247.5	0.0002	237.2	0.011
139.2	0.082	185.3	0.085	232.7	0.0009	222.1	0.001
133.4	0.0191	179.6	0.0112	231.1	0.0008	222.0	0.001
131.4	0.1567	173.2	0	229.9	0	221.5	0
130.7	0.0911	172.9	0.009	228.1	0.0459	213.8	0.0029
121.7	0.0214	167.4	0	219.8	0.0002	213.7	0.0028
121.4	0.071	167.3	0.0642	206.5	0	205.0	0
118.8	0.0341	165.8	0.02	200.6	0.0063	205.0	0
118.6	0.0023	163.6	0.0007	188.6	0.0279	197.4	0.0013
117.2	0.0009	157.9	0.0005	173.8	0.1771	195.2	0.0019
116.0	0.0059	152.0	0.037	167.5	0.0123	195.2	0.0019
114.9	0.067	150.7	0	167.2	0.0064	193.9	0.0076
112.3	0.0094	143.6	0	166.4	0.0007	193.8	0.0075
112.0	0	142.0	0.0836	165.4	0	192.3	0
111.0	0.037	140.5	0.4635	164.6	0	190.2	0.0085
110.3	0.0068	131.0	0	162.0	0.0002	190.2	0.0083
109.3	0.073	130.9	0.0107	155.5	0	187.1	0.015
105.8	0.0404	130.1	0.0358	155.1	0.0004	186.3	0
105.4	0.4533	126.0	0.0663	155.0	0.0017	185.0	0.0145

Table A3. Peak wavelengths and oscillators strengths (*f*) for the first 30 excited states of I_2O_2, I_2O_3, and I_2O_4 at the TD/B3LYP/G2 level of theory.

I_2O_2		**I_2O_3**		**I_2O_4**	
λ / nm	*f*	λ / nm	*f*	λ / nm	*f*
758.1	0.0063	518.9	0	676.5	0.0051
563.0	0	455.5	0.0045	366.0	0.0039
480.6	0.0062	335.2	0.034	344.7	0.0008
367.6	0.0052	334.6	0.0006	323.6	0.0348
338.9	0.0108	297.5	0.0046	319.4	0.0375
306.4	0.0478	286.1	0.0025	291.7	0.0342
300.0	0.0009	265.6	0.0061	287.3	0.0017
275.3	0.0358	258.6	0.0419	280.1	0.079
270.3	0.0047	240.7	0.0532	267.9	0.0085
257.1	0.0163	236.0	0.0009	253.3	0.0124
255.4	0.0017	229.0	0.0068	248.1	0.0082
252.7	0.1031	227.5	0	241.0	0.0058
226.1	0.0106	225.7	0.002	237.0	0.0116
219.1	0.0049	223.6	0.0002	231.6	0.0059
200.2	0.0081	217.4	0.0005	228.1	0.0086
199.3	0.0406	215.7	0.0129	225.9	0.001
192.8	0.0187	214.7	0.0169	218.9	0.0145
186.8	0.0034	211.4	0.0039	216.4	0.0101
184.6	0.0041	209.0	0.0332	213.8	0.0181
184.1	0.009	200.7	0.0183	209.6	0.0124
179.0	0.0667	199.1	0.0019	207.6	0.002
177.8	0.0844	197.1	0.1393	206.8	0.0026
177.4	0.0251	190.5	0.0454	202.3	0.0031
172.6	0.0911	185.7	0.0031	199.1	0.0044
170.0	0.0251	175.2	0.0321	197.3	0.0016
168.5	0.007	174.6	0.0031	196.3	0.0101
165.2	0.0301	170.2	0.1018	194.1	0.0283
162.7	0.0146	169.6	0.0256	193.7	0.0071
162.1	0.0058	168.9	0.062	191.9	0.0036
161.2	0.091	167.3	0	190.3	0.0036

Table A4. Peak wavelengths and oscillators strengths (*f*) for the first 30 excited states of I_3O_6 linear, I_3O_6 cyclic, I_3O_7 linear and I_3O_7 cyclic at the TD/B3LYP/G2 level of theory.

I_3O_6 linear		**I_3O_6 cyclic**		**I_3O_7 linear**		**I_3O_7 cyclic**	
λ / nm	*f*	λ / nm	*f*	λ / nm	*f*	λ / nm	*f*
1010.2	0.0052	1235.0	0	880.9	0.0002	643.1	0.0001
554.6	0.0095	850.6	0.0067	782.1	0.0005	546.0	0.0287
486.0	0.0242	771.7	0.0023	657.6	0.0001	517.8	0.0002
467.9	0.0005	630.7	0.0001	606.3	0.0001	434.1	0.0022
452.6	0.0123	550.4	0.0229	601.9	0.0007	427.1	0.0003
432.5	0.0002	531.2	0.0001	542.8	0.002	389.5	0.0014
424.1	0.0032	518.5	0	529.3	0.0006	386.1	0.0002
416.0	0.014	462.3	0.0001	490.3	0.0089	364.3	0.0004
403.2	0.0047	433.1	0	479.5	0.005	357.1	0.0002
390.8	0.0033	392.7	0.0004	462.5	0.0089	355.6	0.0001
384.2	0.004	387.8	0.0082	382.9	0.0054	351.9	0.002
379.0	0.0031	371.9	0.0002	376.9	0.0006	347.7	0.0005
361.9	0.0203	363.2	0	364.0	0.001	343.5	0.012
353.4	0.0154	354.1	0.0008	353.5	0	338.7	0.0042
347.0	0.0009	351.2	0.0013	340.1	0.0052	334.2	0.0039
344.8	0.0159	349.1	0.0002	333.9	0.0004	331.7	0.0108
336.5	0.0117	339.8	0.0023	331.7	0.0032	329.8	0.0001
329.5	0.0073	333.3	0.0001	311.0	0	326.3	0.001
323.7	0.0024	332.1	0	305.6	0.082	322.0	0.0022
321.8	0.0044	325.4	0.0026	304.5	0.0737	320.2	0.0026
317.7	0.0015	325.0	0.0009	300.9	0.0001	314.1	0.0019
316.2	0.0079	323.1	0.0017	295.3	0.0005	310.1	0.0031
301.6	0.0035	318.5	0.0081	290.8	0.0013	302.7	0.0004
297.6	0.0115	315.8	0.008	290.2	0.0013	298.5	0.0003
295.8	0.002	311.9	0.0028	289.9	0.0028	297.4	0.0007
295.1	0.0234	309.0	0.0521	284.9	0.0055	293.3	0.0015
290.2	0.0001	308.0	0.0011	279.1	0.0005	292.6	0.0004
284.7	0.0015	306.2	0.0015	275.3	0	289.0	0.004
282.3	0.0102	302.8	0.0014	274.8	0.0018	285.4	0.0034
279.0	0.0059	299.0	0.0014	269.4	0.0003	282.2	0.0025

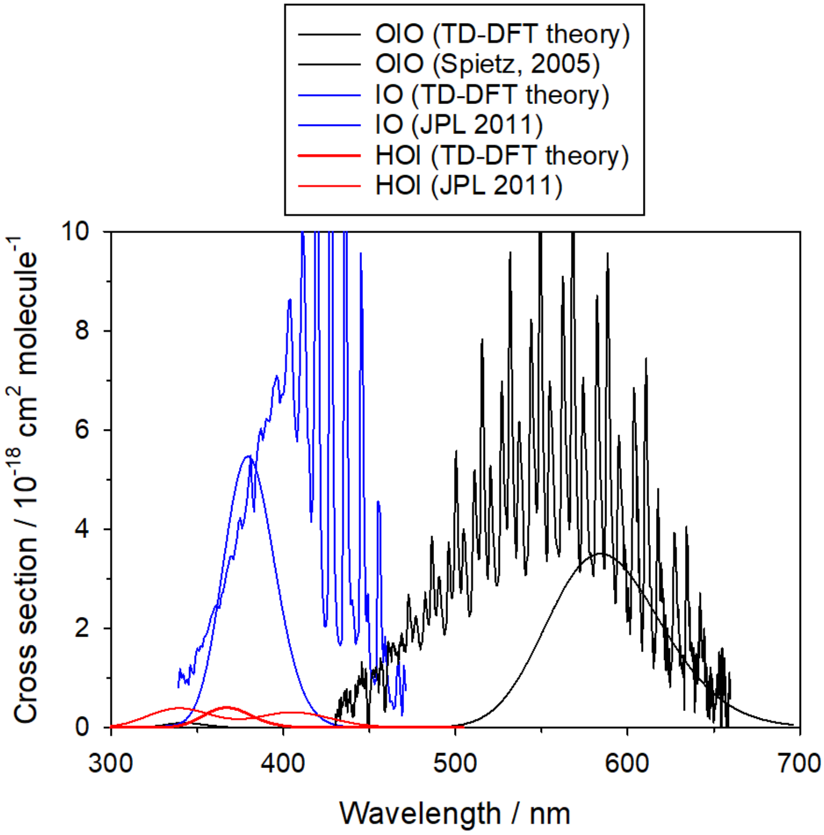

Figure A2: Experimental absorption cross sections of IO (Sander et al., 2011), OIO (Spietz et al., 2005) and HOI (Sander et al., 2011) and absorption spectra calculated with the TD-DFT method (this work).

Field Code Changed

Field Code Changed

APENDIX B. Photofragmentation of I_xO_y species

The photofragmentation of I_xO_y species to daughter ions in the photoionization chamber of the detection apparatus necessitates careful experimentation in order to ensure that any photodepletion of a species of interest is solely due to its 355 nm or 532 nm photolysis in the flow tube, and not obscured by the daughter ions of larger I_xO_y species. To elucidate the optimal window for investigating photodepletion of each species, time resolved mass-spectra were recorded for each set of experimental conditions (Figure 5). From the kinetic information, it is then possible to inspect the averages of the mass spectra within these windows to ensure that the species of interest is present, but larger I_xO_y species are not, as shown in Figure B1. By ensuring no larger I_xO_y species are present, it follows that for a species of interest, only parent ions of the species are contributing to the signal intensity within that time window, and that no contribution to the recorded signal is coming from daughter ions. Note that the signals shown in Figure 5 and Figure B1 are not accumulated for extended periods of time, and as such are relatively noisy. Long accumulation times and corresponding large signal to noise ratios are unnecessary for these experiments, since the objective is simply to elucidate optimal time-delays within which photodepletion experiments are carried out, (photodepletion experiments are typically carried for ~10× as many accumulations) and are carried out prior to an experimental session. It should be noted also that the optimal timescales such as those shown in Figure 5 and Figure B1, vary depending on the concentration of IO formed at the beginning of the reaction sequence, and since the reactions which facilitate the stepwise formation of the higher oxides are second-order, even modest changes in [IO] at early times can result in significant changes to the appearance times of the different species of interest.

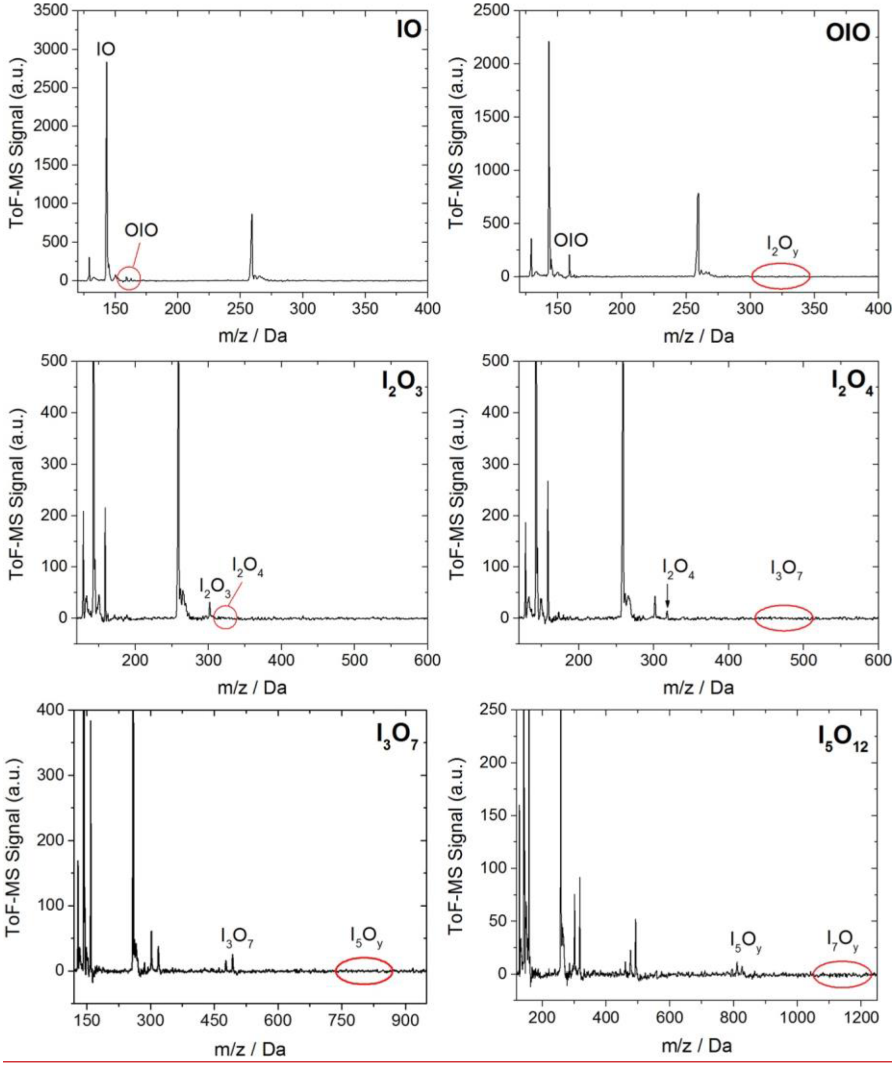

Figure B1: Mass spectra corresponding to the optimised time delays shown in Figure 5. The plots are generated by averaging the signal obtained for each mass over the 5 ms window. The species of interest is given in the top right corner of each spectrum.